Polar solvent-induced spontaneous nano-foaming for synthesizing ultra-high-performance polyamide nanofiltration membranes

Li Ares Wang[†], Huimin He[‡], Qimao Gan[†], Hao Guo[†,§], Zhe Yang[†], Lizhi Xu[‡], Chuyang Y. Tang*[,†]

[†]Department of Civil Engineering, The University of Hong Kong, Hong Kong SAR 999077, China.

[‡]Department of Mechanical Engineering, The University of Hong Kong, Hong Kong SAR 999077, China.

[§]Institute of Environment and Ecology, Shenzhen International Graduate School, Tsinghua University, Shenzhen, 518055, China.

*Corresponding Author:

Chuyang Y. Tang, tangc@hku.hk

■ ABSTRACT

Nanofiltration membranes with both high water permeance and selectivity are perpetual pursuit for their applications in water purification. However, these two critical attributes are considered to be mutually exclusive. Here, we introduce a polar solvent of dichloromethane, instead of the apolar hexane used for decades, as the organic phase for membrane interfacial polymerization synthesis to solve this dilemma. By interfacing a polar solvent as an organic phase with a solvent-resistant aramid nanofibrous hydrogel film as the water phase, monomer enrichment in the reaction zone leads to a polyamide nanofiltration membrane with densely distributed nanobubble features, enhanced nanoporosity, and loosened backbone. Benefiting from these structural features, the resulting membrane exhibits superior properties of the combination of high water permeance (52.7 L m^{-2} h^{-1} bar^{-1}) and selectivity (water-Na_2SO_4: 36 bar^{-1}, NaCl-Na_2SO_4: 357), outperforming traditional nanofiltration membranes. We envision this novel technology involving polar solvent systems and water phase of nanofibrous hydrogel would provide new opportunities to membrane development for environmental engineering.

KEYWORDS: *nanofiltration polyamide membranes, polar-solvent assisted interfacial polymerization, nanobubble features, monomer enrichment*

SYNOPSIS: Polar-solvent assisted interfacial polymerization endows densely distributed nano-foamy structures toward enhanced water permeance without sacrificing selectivity stemming from PIP enrichment in the reaction zone.

■ INTRODUCTION

Polyamide (PA) thin film composite (TFC) nanofiltration (NF) membranes, as the gold standard of low-energy and high-throughput technology, have been widely studied for water and wastewater treatment[1-3]. Over the past decades, extensive efforts have been dedicated to PA design and modification for enhancing NF performance[4-11]. A highly permeable NF membrane without compromising its selectivity is of critical importance to achieve substantial energy saving and expand up-scalable applications[12]. Reducing membrane thickness, e.g., to sub-10 nm, could be an effective way to lower the water transport resistance, leading to a high permeance in the context of reverse osmosis (RO)[13, 14]. However, this strategy is less applicable for the NF realm, as overly reduced membrane thickness may incur the formation of less-crosslinked PA with weakened salt rejection[15]. Alternatively, roughening the surface morphology of NF membranes becomes a promising strategy for improving pure water productivity by increasing effective permeable area[16, 17] and optimizing transport pathways[18-20].

To date, various approaches have been developed to tailoring the membrane morphological features through additive[21-23], patterned substrate[24], or sacrificial template methods[25, 26], leading to an enhanced water permeance benefiting from the crumpled surface of modified NF PA membranes. Nevertheless, these membranes suffer from a reduced selectivity to some extent, rendering rare results surpassing the longstanding upper bound tradeoff line[2, 27, 28]. For TFC RO membrane synthesis, a spontaneous nano-foaming mechanism, arisen by the release of nanosized gas bubbles during the exothermic interfacial polymerization (IP), is responsible for the typically

56 “ridge-and-valley” motifs[16]. Such exceptional process needs high enthalpy reaction
57 commonly with the highly reactive amine monomer, which is applicable for RO
58 membranes synthesized from *m*-phenylenediamine (MPD). Despite that spontaneous
59 nano-foaming has been rarely reported for NF membranes fabricated with piperazine
60 (PIP)–a far less reactive amine monomer[29, 30], we hypothesize that enriching PIP in the
61 reaction zone for IP can trig this mechanism, resulting in nanovoid-containing rough
62 polyamide surface to achieve high NF separation performance.

63 Previous research shows that the IP reaction occurs predominantly in the apolar
64 organic phase–hexane (Fig. 1a)[15]. The inner reaction zone, where both amine monomer
65 (PIP) and acyl chloride monomer (trimesoyl chloride, TMC) co-exist, exhibits limited
66 PIP amount due to its intrinsic polar structure. Here, to facilitate PIP enrichment in
67 organic phase, a common polar organic solvent, dichloromethane (DCM), was selected
68 to construct an immiscible interface for PA fabrication for the first time (Fig. 1b). A
69 solvent-resistant aramid nanofibrous (ANF) hydrogel was well selected as the water
70 phase to enable the membrane preparation process with sufficient PIP supply. The polar
71 nature of DCM facilitates the PIP trans-across the interface, and the PIP enrichment in
72 the reaction zone caused by DCM endows the formation of nanobubble-like pattern.
73 Based on the molecular dynamics (MD) simulations, our study reveals the expanded
74 interfacial domain using DCM, incorporated with the reduced energy penalty,
75 suggesting the favorable behavior for PIP to enter the polar organic phase. All these
76 results provide a mechanistic insight on PIP enrichment and a robust method of

77 membrane fabrication with novel nanobubble pattern for ultra-permeable and ultra-
78 selective membranes for various separation aims.

■ RESULTS AND DISCUSSION

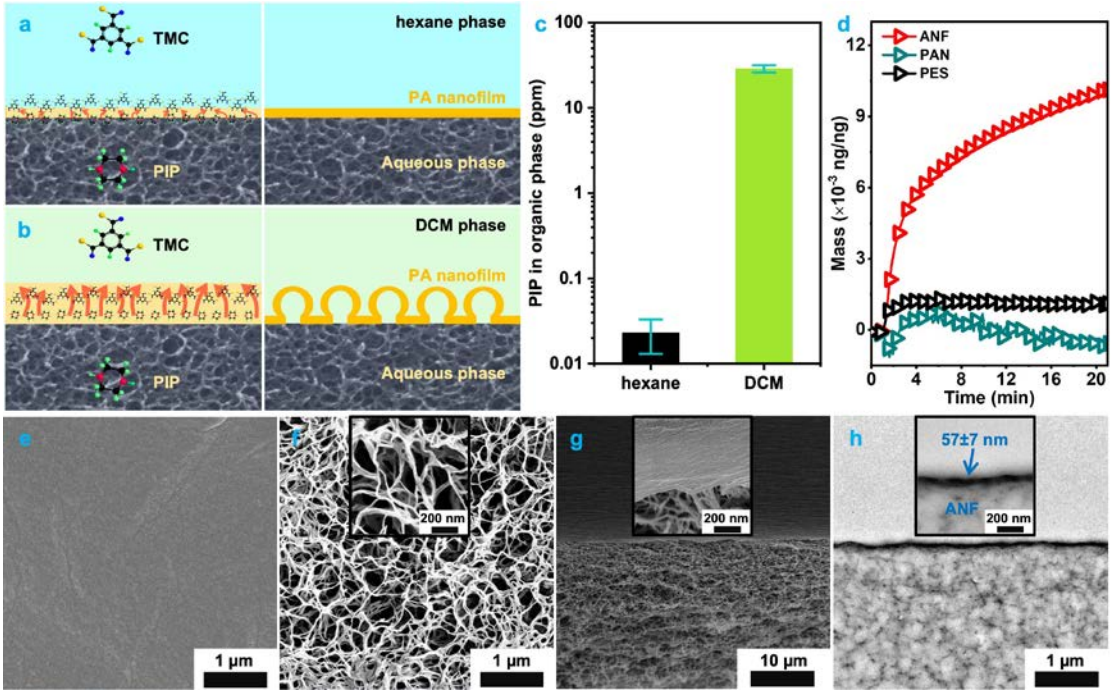

Fig. 1 Fabrication of TFC PA membrane using DCM. (a, b) schematic of flat and nano-foamed PA prepared on hydrogel. (c) Detected PIP concentration in the organic phase by ultraviolet-visible (UV-Vis) spectrophotometer. The collection details are shown in Fig. S3-6. (d) PIP adsorption curves of ANF hydrogel (made of Kevlar yarns[31]), polyacrylonitrile (PAN) and polyester sulfone (PES) obtained using a quartz crystal microbalance with dissipation (QCM-D, the overtone number is 3). Each polymer was spin-coated onto Au wafer, and the coated amount calculated based on the Sauerbrey equation[32-34] was identical. (e, f, g) Top surface, rear surface, and cross-sectional scanning electron microscopy (SEM) images of the cast ANF hydrogel with the corresponding high magnification inset. (h) Cross-sectional transmission electron microscopy (TEM) image of ANF with its high magnification inset.

Fabrication of nano-foamed TFC NF PA membrane based on a solvent-resistant hydrogel. Conventional NF PA membranes formed via apolar hexane has a flat surface morphology (Fig. 1a). In our pioneer work, we discovered that PA membranes fabricated by a polar solvent of DCM have novel nanobubble-like features (Fig. 1b). Fabrication of PA by interfacial polymerization is a rate-limited process[7] majorly controlled by the slow diffusion rate of PIP into the organic phase. Markedly, Fig. 1c reveals that the amount of PIP in DCM is 3 orders of magnitude higher than that in hexane, suggesting that the polar DCM greatly enhances the partition of PIP into the

reaction zone. Meanwhile, the ANF substrate has much more affinity with higher PIP absorption amount (Fig. 1d) compared with other conventional polymeric substrates such as PES and PAN.

SEM and TEM images (Fig 1e-h) show that the casted ANF substrate has special sponge-like fibrous structures with a denser skin layer on the top and a more porous layer underneath. During the exothermic process of IP atop the ANF, a large amount of released heat coupled with gas product caused by enriched monomer would penetrate toward the organic phase (as the opposite direction is blocked by ANF), which would favor the formation of nanobubble pattern.

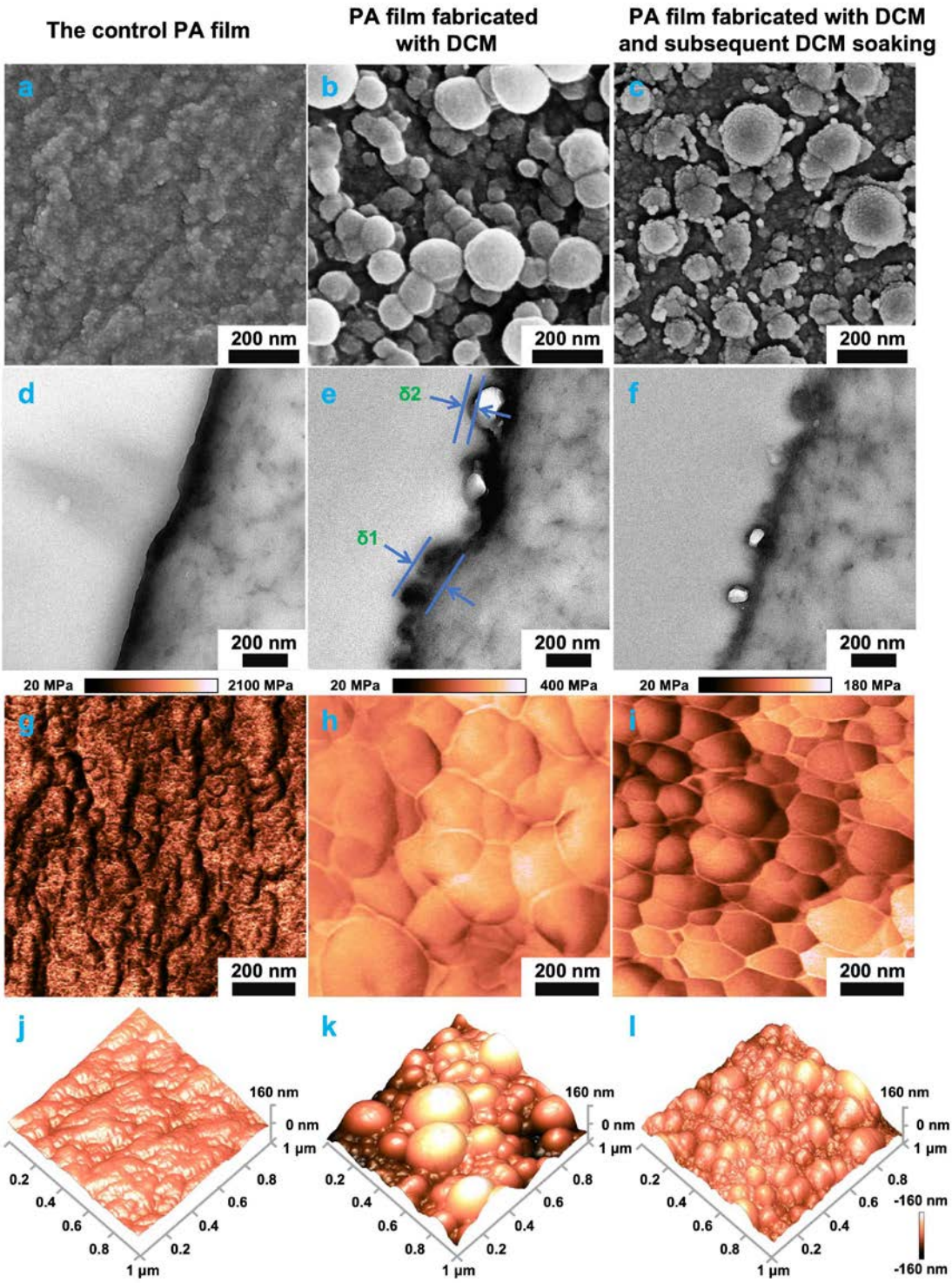

Fig. 2 Morphology of the PA membranes. (a, b, c) High magnification surface SEM images, (d, e, f) cross-sectional TEM images, (g, h, i) surface Young's modulus based on atomic force microscopy (AFM), and (j, k, l) surface AFM height profile of PA rejection layer fabricated with hexane (control), DCM, and subsequent DCM soaking, respectively. The corresponding TMC and PIP concentrations used for the IP reaction are 0.5% w v^{-1} and 0.04% w v^{-1}, respectively. The δ1 and δ2 shown in Fig. 2e denotes apparent thickness and intrinsic thickness of PA rejection layer, respectively.

Nanobubble-like morphology of the TFC PA membranes. The morphology of the fabricated TFC PA membranes was extensively investigated by SEM, TEM, and AFM after critical point drying (CPD) (Fig. 2). To exclude the effects of dehydration, the surface of membrane fabricated with DCM was also characterized by scanning electron cryomicroscopy (cryoSEM) under hydrated condition (see Fig. S7). The original morphology of hydrated sample is the same as that after CPD treatment, confirming that the CPD process maintains the original morphology of membranes. Specifically, the membrane prepared with hexane exhibits a flat surface (Fig. 2a). In contrast, the surface and cross-sectional images of SEM and cryoSEM of membranes fabricated with DCM shows the presence of densely distributed spherical structures (Fig. 2b, 2c and Fig. S8-11).

Different from the flat and solid membrane fabricated with hexane (Fig. 2d), the spherical structures for the membranes prepared with DCM are actually hollow inside, as determined by TEM results (Fig. 2e, 2f and Fig. S12-14). Indeed, the unique nanobubble-like morphology is attributed to the effects from both the solvent of DCM and the substrate of ANF hydrogel. When we replace ANF with a PAN substrate for membrane fabrication, only flat surface with minor winkles are observed atop the nascent film (Fig. S13). In this case, PAN substrate exhibits insufficient PIP storage for IP (Fig. 1d).

In order to validate the effects of PIP enrichment on the generation of nanobubble surface features, we further change the concentrations of TMC and PIP for the IP

reaction. Minimum concentrations for TMC (0.2% w v^{-1}) and PIP (0.04% w v^{-1}) monomers are required to achieve the transformation from a flat surface with rare spread nodules to a unique surface with extensive nanobubbles (see Fig. S8-10). This result can be explained as low monomer concentration in two immiscible phases will lower the monomer concentration in the reaction zone, which will then cause the mild IP process without enough thermal energy released to produce the nanobubble features.

Film thickness is another critical parameter for the separation performance. In general, through dissolving the polysulfone support layer with dimethylformamide (DMF), the apparent thickness of PA rejection layer can be determined based on the analysis of AFM surface topography. However, we found that the PA rejection layer can hardly be separated from ANF substrate in our study due to the solvent-resistant nature of ANF and a robust adhesion stemmed from similar chemical compositions between them[31] (Fig. S16-18, Table S1). Compared with the apparent thickness, the intrinsic thickness–the actual thickness of PA excluding nanovoid–reveals an inherent relation with the separation performance[35]. Hence, we use cross-sectional TEM results (Fig. 2d, 2e, and 2f) to estimate the intrinsic thickness of the fabricated PA layer. The intrinsic thickness of PA layer fabricated with hexane was determined by subtracting PA-ANF layer of ~122 nm (Fig. 2d) with the ANF layer of ~57 nm (Fig. 1h), resulting in the intrinsic thickness of about 65 nm. After replacing hexane with DCM for IP process, the intrinsic thickness of fabricated PA is reduced to ~ 45 nm (Fig. S14a). This thickness can be further reduced to ~ 15 nm (Fig. S14b) by soaking the membrane fabricated in

DCM overnight to remove the unreacted monomers and loosely attached oligomers–a process known as solvent activation[13, 36]. These results confirm that a thinner PA rejection layer is obtained with DCM and subsequent solvent activation, which might contribute to a high water permeance due to the corresponding short water transport distance.

In addition, the surface Young's modulus of TFC PA membranes were measured by AFM (Fig. 2g-i, and Fig. S19). The control flat membrane has a high modulus value in the range of 250-2000 MPa. In comparison, the crumpled membrane fabricated with DCM exhibits a markedly decreased Young's modulus between 125-250 MPa, which can further decrease to 20-125 MPa after solvent activation. We ascribe these findings to the widespread nanovoids underneath and loose backbone resulted from the strong dissolution of DCM to the PA oligomer. A loose PA backbone typically can be estimated based on the calculated mean effective pore size[37], resulting from the rejection of neutral solutes (Fig. S20 and S21). Specifically, the calculated mean effective pore radius of PA membrane prepared with hexane is 2.6 Å, while that with DCM is 2.9 Å and further increase to 3.3 Å for subsequent solvent activation (see Table S2).

Another solid information on the nanofoamed patterns was provided by AFM height and phase images (Fig. 2j, 2k, 2l, Fig. S22-24). The root mean square roughness of membrane fabricated with DCM (Ra = 79.8 nm, Fig. S22b) shows apparently high value compared with the control (Ra = 18.2 nm, Fig. S22a). After solvent activation, a

decreased Ra of 35.6 nm might result from shrunken (Fig. S23c) and more evenly distributed nanobubbles.

Overall, a PA rejection layer with higher specific surface, thinner thickness, and looser backbone is achieved through the combination of a polar DCM and ANF substrate.

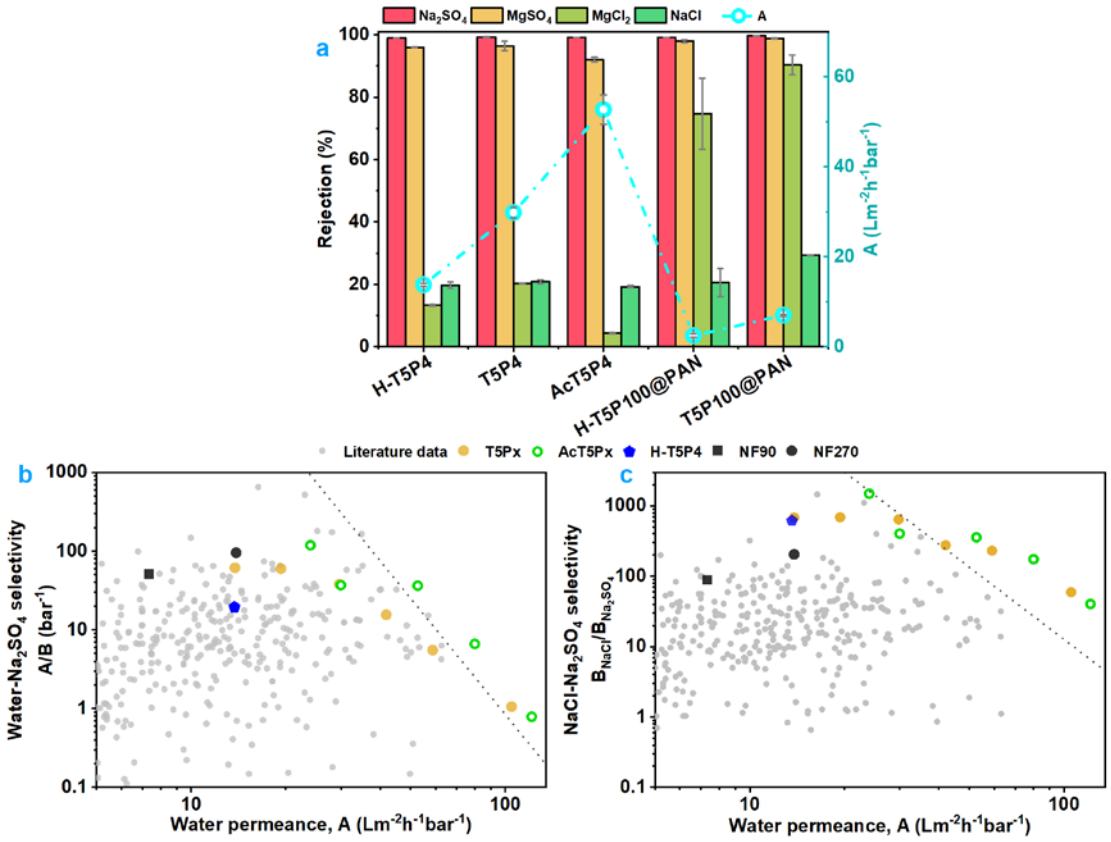

Fig. 3 Separation performance of TFC membranes. (a) Rejection of various salts and pure water permeance of TFC PA membranes. (b, c) Upper bound lines for water-Na_2SO_4 selectivity vs. water permeance and Na_2SO_4-NaCl selectivity vs. water permeance, respectively. The reported literature data for the upper bound figures, denoted as grey dot (~ 400), can be found in the Mendeley Data in ref.[2]. T5Px represents TFC membranes fabricated atop ANF hydrogel with DCM using 0.5% w v^{-1} for TMC, with x (= 1, 2, 3, 4, 5, 6) indicating the PIP concentration (0.01, 0.02, 0.03, 0.04, 0.05, and 0.06% w v^{-1}, respectively). AcT5Px denotes DCM activated T5Px membranes. NF90 and NF270 are two types of commercial TFC NF membranes. For TFC membranes prepared on the PAN substrate, H-T5P100@PAN and T5P100@PAN denote the membranes fabricated using 0.5% w v^{-1} TMC and 1% w v^{-1} PIP with hexane and DCM as the organic phase, respectively.

Highly permeable and selective property. The pure water permeance of TFC NF PA membranes and rejection of various salts (Na_2SO_4, $MgSO_4$, $MgCl_2$ and NaCl) are shown in Fig. 3, Fig. S25 and Fig. S26. Specifically, as shown in Fig. 3a, the pure water permeance of the membrane fabricated based on polar DCM increases by 116% compared with the control (13.8 L m^{-2} h^{-1} bar^{-1}). After further solvent activation, the permeance of the membrane is nearly tripled compared with the control, which can be attributed to the thin and loose backbone in addition to the void-containing nano-foamed structure. According to the results of neutral molecule cut-off (see Table S2), mean pore size is increased from 2.6 for H-T5P4 to 3.3 Å for AcT5P4. Similar to its use in the organic solvent nanofiltration realm[13], the effect of DCM activation on water permeance enhancement can be attributed to the dissolution of unreacted monomers and PA oligomers. Interestingly, the nanoscale homogeneity is improved with the use of DCM in IP and the subsequent solvent activation[8, 38], with the geometric standard deviation σ_p progressively reduced from 2.0 to 1.6. This enhanced nanoscale homogeneity explains the high Na_2SO_4 rejection of the membrane fabricated with DCM (99.3%) and subsequent DCM activation (99.2%), despite the increased mean pore size.

We also prepared PA membranes on another solvent-resistant substrate (PAN). Compared with that formed using hexane (H-T5P100@PAN), the membrane prepared using DCM as the organic solvent (T5P100@PAN) also show substantial improvement in water permeance yet similar or slightly improved salt rejection, further confirming the beneficial effect of the enlarged pore radius (Fig. S27, Table S3). Nevertheless,

compared to their counterparts prepared on ANF (H-T5P4 and T5P4, featuring nano-foamed structures (Fig. 2)), the membranes prepared on PAN (H-T5P100@PAN and T5P100@PAN, with smooth surface morphology (Fig. S15)) show much lower water permeance, underpinning the critical contribution of the nanovoids toward membrane permeance[18].

More detailed separation performance of TFC NF PA membranes fabricated with DCM with various monomer concentration can be found in Fig. S25. After activation with DCM, membranes exhibit larger pore radius (Table S2), leading to a greatly enhanced water permeance. However, amine monomer with lower content participating in IP process might lead to a backbone with plenty of uncross-linked oligomers, which can be dissolved by DCM activation and result in a rapid deterioration on salt separation property (Fig. S25). In this study, when the concentration of PIP used for TFC PA membrane fabrication is higher or equal to 0.04% w v^{-1} (Fig. S25), salts rejection keeps stable even with overnight DCM soaking. This suggests an effectively cross-linked PA matrix, which is verified by XPS results (Fig. S17, S18 and Table S1) and -COOH density characterization (Table S4). In addition, a stable rejection and permeance can also be observed for membranes fabricated with DCM and subsequent activation over a 14-day operation (Fig. S28).

A standard method to assess the separation performance of TFC PA membranes is to plot the membranes in the state-of-the-art permeance-selectivity trade-off figure. Fig. 3b and Fig. 3c benchmark the performance data of the membranes made in this study

against data reported in the literature, including ~ 400 lab-made TFC membranes as well as commercial NF membranes (NF90 and NF270, see Table S5). Remarkable transcending results, as shown in permeance-water/Na_2SO_4 selectivity (A-A/B_{Na2SO4}) and permeance-NaCl/Na_2SO_4 selectivity (A-B_{NaCl}/B_{Na2SO4}) figures, come from TFC PA membranes prepared with DCM. The superiority is obviously ascribed to high water permeance with effective salts rejection stemmed from the comprehensive effects of the chemical structure, surface morphology, nanoscale homogeneity and the intrinsic thickness of the membranes.

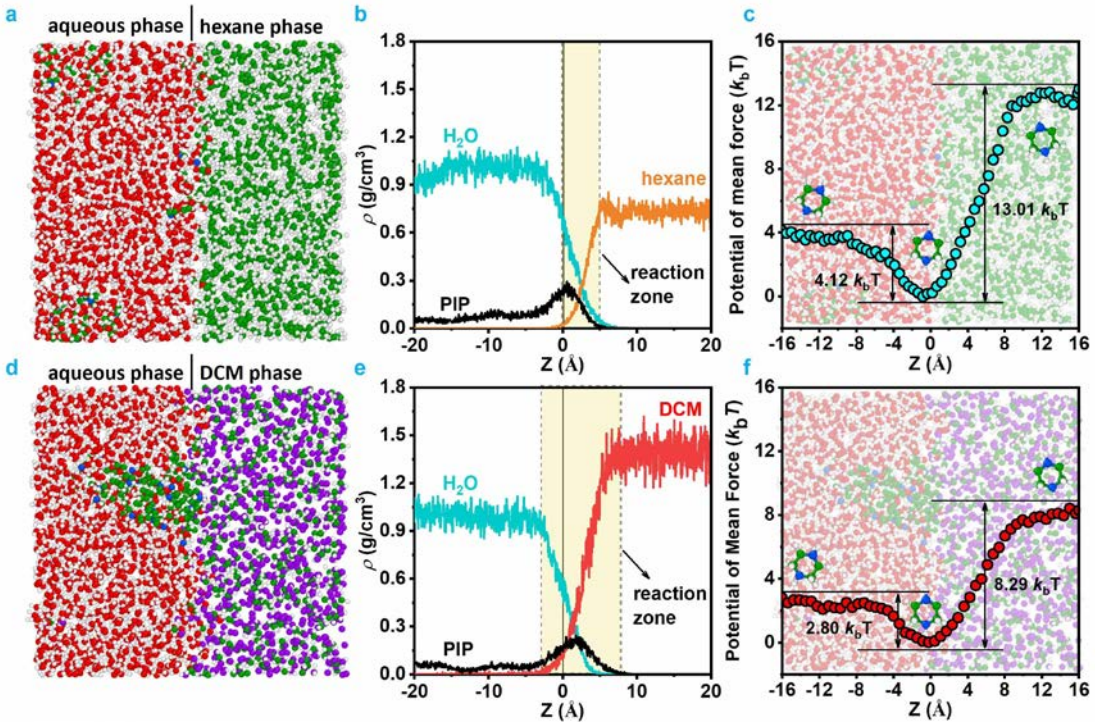

Fig. 4 Distribution of components and the energy barrier of PIP transport at hydrogel/hexane and hydrogel/DCM interface. (a) Hydrogel/hexane interface. (b) Mass density distribution of components (H_2O, hexane and PIP) at the equilibrium state. (c) The potential of mean force (PMF) calculation with the PIP at different locations along the Z coordinate in hexane system (control). (d) Hydrogel/DCM interface. (e) Mass density distribution of components (H_2O, DCM and PIP) at the equilibrium state (f) The PMF calculation with the PIP in DCM system. The number of H_2O, Kevlar, PIP, hexane and DCM in the control system and DCM system for mass density distribution can be found in Table S6, while that for PMF is shown in Table S7.

Nano-foaming mechanism. Molecular dynamic (MD) simulation is a widely adopted tool for the analysis of complex and rapid IP process. During IP, the actual PIP content in the reaction zone has critical influence on the formation of PA film[7, 15]. To properly elucidate the transportation of PIP across the immiscible phases, composite systems (Fig. 4a and Fig. 4d) related with monomer distributions (Fig. 4b and Fig. 4e) and the corresponding PMF (Fig. 4c and Fig. 4f) were built. The initial configurations of systems can be found in Fig. S30, and the detailed process of system construction is shown in Supplementary Information Section 5. As shown in Fig. 4, the reaction zone in DCM system (Fig. 4e) is obviously expanded compared with the hexane system (Fig. 4b), as a small quantity of water and DCM transfer into the opposite phase and the mass density distribution curve of PIP spreads more into the DCM phase.

In addition, compared with the control system (Fig. 4b), the PIP maximum density peak in DCM system shifts more toward the organic phase (see Fig. 4e**,** Fig. S31, Movie S1 and S2). This result is in good agreement with the experimental observations on PIP partitioning between the water/organic phases (Fig. 1c), confirming that polar DCM has a higher affinity to the PIP molecules than the apolar hexane. The affinity of DCM to PIP was further investigated using the UV-Vis spectroscopy. Compared with PIP dissolving in hexane, the PIP/DCM solution exhibits a hypsochromic shift behavior, as evidenced by the observed shift from 273 nm to 231 nm (Fig. S3, Fig. S4, and Table S8). In fact, the affinity of DCM to PIP can be attributed to the polar nature of DCM, which is capable of forming hydrogen bonds with polar PIP molecules. Benefiting from

the affinity, the calculated self-diffusion coefficient of PIP in the DCM system exhibits notably higher value than that in the control system (Fig. S32). In summary, the polar nature of DCM facilitates the extension of reaction zone and PIP diffusion across the interface, leading to the PIP enrichment in the reaction zone.

The PIP enrichment behavior can be further elucidated by PMF calculation. As shown in Fig. 4c and Fig. 4f, the MD simulation reveals that the PIP monomers tend to stay at the immiscible oil/water interface where both cases have the lowest PMF, suggesting the interfacial accumulation phenomenon (i.e., the maximum density peak of PIP). The concentration gradient caused by interfacial accumulation then drives the PIP monomers transferring to the organic phase. Compared with hexane system, the energy penalty for PIP to enter the DCM bulk was greatly reduced, from 13.01 to 8.29 K_bT. This can be explained by enhanced affinity between polar PIP and polar DCM resulting from hydrogen bonds. Due to the reduced energy barrier, the diffusion of PIP to the DCM bulk becomes more energetically favorable, which then cause the shift of the maximum density peak of PIP to the DCM bulk and facilitate the PIP enrichment in the reaction zone.

During the IP procedure, PIP monomers diffuse into the reaction zone to fulfill the IP reaction. The actual PIP content in the reaction zone, which is highly constrained by the organic phase, largely regulates the IP kinetics. As an exothermal reaction[15, 16, 39], faster diffusivity of PIP with an expanded reaction zone and several orders of magnitude higher partitioning amount (Fig. 1c) yields a huge amount of heat release (see Fig. S34,

294 Movie S3). Surrounded by the DCM matrix, the newly formed soft PA film, blown with
295 in-situ generated nano-gas vapor (Fig. S35), forms a densely distributed nanobubble
296 pattern.

■ ASSOCIATED CONTENT

Supporting Information

The Supporting Information is available free of charge at.

Fabrication, PIP diffusion process, morphology and structure, separation performance and structure, MD Details, and other supplementary experiments (PDF and movies)

■ AUTHOR INFORMATION

Corresponding Author

Chuyang Y. Tang − *Department of Civil Engineering, The University of Hong Kong, Pokfulam, Hong Kong SAR 999077, P. R., China;* orcid.org/0000-0002-7932-6462; Phone: +852 28591976; Email: tangc@hku.hk

Authors

Li Ares Wang − *Department of Civil Engineering, The University of Hong Kong, Pokfulam, Hong Kong SAR 999077, P. R., China*

Huimin He − *Department of Mechanical Engineering, The University of Hong Kong, Pokfulam, Hong Kong SAR 999077, P. R., China*

Qimao Gan − *Department of Civil Engineering, The University of Hong Kong, Pokfulam, Hong Kong SAR 999077, P. R., China*

Hao Guo − *Institute of Environment and Ecology, Shenzhen International Graduate School, Tsinghua University, Shenzhen, 518055, P. R., China*

Zhe Yang − *Department of Civil Engineering, The University of Hong Kong, Pokfulam, Hong Kong SAR 999077, P. R., China*

Lizhi Xu − *Department of Mechanical Engineering, The University of Hong Kong, Pokfulam, Hong Kong SAR 999077, P. R., China*

Notes

The authors declare no competing financial interest.

■ ACKNOWLEDGMENTS

The work was substantially supported by a grant from the Research Grants Council of the Hong Kong Special Administration Region, China (GRF 17206122). We also acknowledge the partial funding support from Innovation and Technology Fund of the Hong Kong Special Administration Region, China (GHP/181/20GD). The QCM-D measurement system was partially funded by The University of Hong Kong (URC Small Equipment Fund). L.X. acknowledges funding support from Research Grants Council (RGC), University Grants Committee (UGC) (Project 17200722, 17200320 and C6004-22Y) and support from Environment and Conservation Fund (project 125/2021).

■ REFERENCES

(1) Elimelech M, Phillip WA. The future of seawater desalination: energy, technology, and the environment. *Science* **2011**, *333* (6043), 712-717.

(2) Yang Z; Long L; Wu C, Tang CY. High Permeance or High Selectivity? Optimization of System-Scale Nanofiltration Performance Constrained by the Upper Bound. *ACS EST Engg* **2021**, *2*, 377-390.

(3) Geise GM. Why polyamide reverse-osmosis membranes work so well. *Science* **2021**, *371* (6524), 31-32.

(4) Gao S; Zhu Y; Gong Y; Wang Z; Fang W, Jin J. Ultrathin polyamide nanofiltration membrane fabricated on brush-painted single-walled carbon nanotube network support for ion sieving. *ACS nano* **2019**, *13* (5), 5278-5290.

(5) Peng H; Zhang WH; Hung WS; Wang N; Sun J; Lee KR; An QF; Liu CM, Zhao Q. Phosphonium Modification Leads to Ultrapermeable Antibacterial Polyamide Composite Membranes with Unreduced Thickness. *Adv. Mater.* **2020**, *32* (23), 2001383.

(6) Liu C; Yang J; Guo BB; Agarwal S; Greiner A, Xu ZK. Interfacial Polymerization at the Alkane/Ionic Liquid Interface. *Angew. Chem. Int. Ed.* **2021**, *60* (26), 14636-14643.

(7) Liang Y; Zhu Y; Liu C; Lee KR; Hung WS; Wang Z; Li Y; Elimelech M; Jin J, Lin S. Polyamide nanofiltration membrane with highly uniform sub-nanometre pores for sub-1 A precision separation. *Nat. Commun.* **2020**, *11* (1), 2015.

(8) Shen L; Cheng R; Yi M; Hung W-S; Japip S; Tian L; Zhang X; Jiang S; Li S,

Wang Y. Polyamide-based membranes with structural homogeneity for ultrafast molecular sieving. *Nat. Commun.* **2022**, *13* (1), 500.

(9) Sarkar P; Modak S, Karan S. Ultraselective and highly permeable polyamide nanofilms for ionic and molecular nanofiltration. *Adv. Funct. Mater.* **2021**, *31* (3), 2007054.

(10) Han S; Zhu J; Uliana AA; Li D; Zhang Y; Zhang L; Wang Y; He T, Elimelech M. Microporous organic nanotube assisted design of high performance nanofiltration membranes. *Nat. Commun.* **2022**, *13* (1), 7954.

(11) Zhao C; Zhang Y; Jia Y; Li B; Tang W; Shang C; Mo R; Li P; Liu S, Zhang S. Polyamide membranes with nanoscale ordered structures for fast permeation and highly selective ion-ion separation. *Nat. Commun.* **2023**, *14* (1), 1112.

(12) Yang Z; Wu C, Tang CY. Making waves: Why do we need ultra-permeable nanofiltration membranes for water treatment? *Water Res. X* **2023**, *19*, 100172.

(13) Karan S; Jiang ZW, Livingston AG. Sub-10 nm polyamide nanofilms with ultrafast solvent transport for molecular separation. *Science* **2015**, *348* (6241), 1347-1351.

(14) Jiang Z; Karan S, Livingston AG. Water transport through ultrathin polyamide nanofilms used for reverse osmosis. *Adv. Mater.* **2018**, *30* (15), 1705973.

(15) Freger V, Ramon GZ. Polyamide desalination membranes: Formation, structure, and properties. *Prog. Polym. Sci.* **2021**, *122*, 101451.

(16) Ma XH; Yao ZK; Yang Z; Guo H; Xu ZL; Tang CYY, Elimelech M. Nanofoaming

of Polyamide Desalination Membranes To Tune Permeability and Selectivity. *Environ. Sci. Technol. Lett.* **2018**, *5* (2), 123-130.

(17) Dai R; Zhou H; Wang T; Qiu Z; Long L; Lin S; Tang CY, Wang Z. Nanovehicle-assisted monomer shuttling enables highly permeable and selective nanofiltration membranes for water purification. *Nature Water* **2023**, *1*, 281-290.

(18) Hu Y; Wang F; Yang Z, Tang CY. Modeling nanovoid-enhanced water permeance of thin film composite membranes. *J. Membr. Sci.* **2023**, *675*, 121555.

(19) Yang Z; Sun P-F; Li X; Gan B; Wang L; Song X; Park H-D, Tang CY. A critical review on thin-film nanocomposite membranes with interlayered structure: mechanisms, recent developments, and environmental applications. *Environ. Sci. Technol.* **2020**, *54* (24), 15563-15583.

(20) Shao S; Zeng F; Long L; Zhu X; Peng LE; Wang F; Yang Z, Tang CY. Nanofiltration membranes with crumpled polyamide films: a critical review on mechanisms, performances, and environmental applications. *Environ. Sci. Technol.* **2022**, *56* (18), 12811-12827.

(21) Yuan B; Wang N; Zhao S; Hu P; Jiang J; Cui J; Zhang X; You M; Lou X, Niu QJ. Polyamide nanofiltration membrane fine-tuned via mixed matrix ultrafiltration support to maximize the sieving selectivity of Li^+/Mg^{2+} and Cl^-/SO_4^{2-}. *Desalination* **2022**, *538*, 115929.

(22) Tan Z; Chen SF; Peng XS; Zhang L, Gao CJ. Polyamide membranes with nanoscale Turing structures for water purification. *Science* **2018**, *360* (6388), 518-

521.

(23) Yang Z; Guo H; Yao ZK; Mei Y, Tang CY. Hydrophilic Silver Nanoparticles Induce Selective Nanochannels in Thin Film Nanocomposite Polyamide Membranes. *Environ. Sci. Technol.* **2019**, *53* (9), 5301-5308.

(24) Yuan B; Zhao S; Hu P; Cui J, Niu QJ. Asymmetric polyamide nanofilms with highly ordered nanovoids for water purification. *Nat. Commun.* **2020**, *11* (1), 6102.

(25) Lu Y; Wang R; Zhu Y; Wang Z; Fang W; Lin S, Jin J. Two-dimensional fractal nanocrystals templating for substantial performance enhancement of polyamide nanofiltration membrane. *Proc. Natl. Acad. Sci. U.S.A.* **2021**, *118* (37), e2019891118.

(26) Wang Z; Wang Z; Lin S; Jin H; Gao S; Zhu Y, Jin J. Nanoparticle-templated nanofiltration membranes for ultrahigh performance desalination. *Nat. Commun.* **2018**, *9* (1), 1-9.

(27) Yang Z; Guo H, Tang CY. The upper bound of thin-film composite (TFC) polyamide membranes for desalination. *J. Membr. Sci.* **2019**, *590*, 117297.

(28) Ritt CL; Stassin T; Davenport DM; DuChanois RM; Nulens I; Yang Z; Ben-Zvi A; Segev-Mark N; Elimelech M, Tang CY. The open membrane database: Synthesis–structure–performance relationships of reverse osmosis membranes. *J. Membr. Sci.* **2022**, *641*, 119927.

(29) Lo R; Bhattacharya A, Ganguly B. Probing the selective salt rejection behavior of thin film composite membranes: A DFT study. *J. Membr. Sci.* **2013**, *436*, 90-

96.

(30) Li S-L; Shan X; Zhao Y, Hu Y. Fabrication of a novel nanofiltration membrane with enhanced performance via interfacial polymerization through the incorporation of a new zwitterionic diamine monomer. *ACS Appl. Mater. Interfaces* **2019**, *11* (45), 42846-42855.

(31) Tanner D; Fitzgerald JA, Phillips BR. The Keviar story—an advanced materials case study. *Adv. Mater.* **1989**, *1* (5), 151-156.

(32) Kanazawa KK, Gordon JG. Frequency of a quartz microbalance in contact with liquid. *Anal. Chem.* **1985**, *57* (8), 1770-1771.

(33) Voinova MV; Rodahl M; Jonson M, Kasemo B. Viscoelastic acoustic response of layered polymer films at fluid-solid interfaces: continuum mechanics approach. *Phys. Scr.* **1999**, *59* (5), 391.

(34) Yang Z; Zhou ZW; Guo H; Yao ZK; Ma XH; Song XX; Feng SP, Tang CYY. Tannic Acid/Fe^{3+} Nanoscaffold for Interfacial Polymerization: Toward Enhanced Nanofiltration Performance. *Environ. Sci. Technol.* **2018**, *52* (16), 9341-9349.

(35) Song X; Gan B; Qi S; Guo H; Tang CY; Zhou Y, Gao C. Intrinsic nanoscale structure of thin film composite polyamide membranes: Connectivity, defects, and structure–property correlation. *Environ. Sci. Technol.* **2020**, *54* (6), 3559-3569.

(36) Solomon MFJ; Bhole Y, Livingston AG. High flux membranes for organic solvent nanofiltration (OSN)—Interfacial polymerization with solvent activation. *J.*

Membr. Sci. **2012**, *423*, 371-382.

(37) Lin J; Tang CY; Huang C; Tang YP; Ye W; Li J; Shen J; Van den Broeck R; Van Impe J, Volodin A. A comprehensive physico-chemical characterization of superhydrophilic loose nanofiltration membranes. *J. Membr. Sci.* **2016**, *501*, 1-14.

(38) Culp TE; Khara B; Brickey KP; Geitner M; Zimudzi TJ; Wilbur JD; Jons SD; Roy A; Paul M, Ganapathysubramanian B. Nanoscale control of internal inhomogeneity enhances water transport in desalination membranes. *Science* **2021**, *371* (6524), 72-75.

(39) Ukrainsky B, Ramon GZ. Temperature measurement of the reaction zone during polyamide film formation by interfacial polymerization. *J. Membr. Sci.* **2018**, *566*, 329-335.

452 ■ **TOC Graphic**

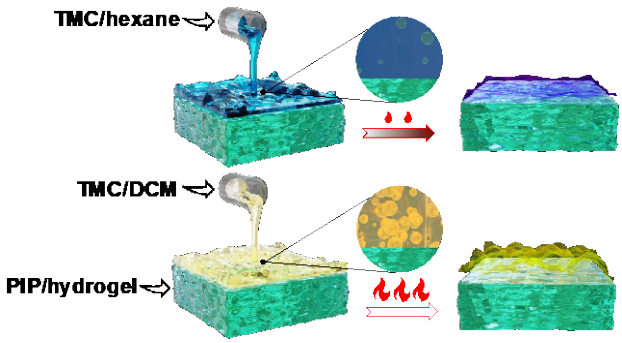

453

Supporting information for

Polar solvent-induced spontaneous nano-foaming for synthesizing ultra-high-performance polyamide nanofiltration membranes

Li Ares Wang[†], Huimin He[‡], Qimao Gan[†], Hao Guo[†,§], Zhe Yang[†], Lizhi Xu[‡], Chuyang Y. Tang*[,†]

[†]Department of Civil Engineering, The University of Hong Kong, Hong Kong SAR 999077, China.

[‡]Department of Mechanical Engineering, The University of Hong Kong, Hong Kong SAR 999077, China.

[§]Institute of Environment and Ecology, Shenzhen International Graduate School, Tsinghua University, Shenzhen, 518055, China.

*Corresponding Author:

Chuyang Y. Tang, tangc@hku.hk

Contents

1. Fabrication

1.1. Materials and chemicals

The Kevlar aramid nanofibers (ANFs) pulp (Type 979) was purchased from DuPont company. Flat sheets including NF90 TFC PA membranes, NF270 TFC PA membranes, and polyacrylonitrile (PAN) substrates (GC-UF0503, ~50,000 Da) were all purchased from Guo Chu Technology (Xiamen, China) Co., Ltd. Dichloromethane (DCM, ACS grade) and dimethyl sulfoxide (DMSO, ACS) were obtained from STANDHILL Technology (Hong Kong, China) Co., Ltd. 1,3,5-Benzenetricarboxylic acid chloride (TMC, 98%) was collected from Bide Pharmatech (Shanghai, China) Co., Ltd. Piperazine (PIP, 99%) and PAN polymer powder (average Mw~150,000, AR) were purchased from Sigma-Aldrich (US). Potassium chloride (KCl, ≥99.99%) was obtained from Shanghai Aladdin Bio-Chem Technology Co., Ltd. Sodium sulfate (Na_2SO4, AR), sodium chloride (NaCl, AR), magnesium sulfate ($MgSO_4$, AR), magnesium chloride ($MgCl_2$, 99%), glycerol (AR), glucose (AR), sucrose (AR), and dextran (Mw ~ 1,000, BR) were all obtained from Dieckmann (Hong Kong, China) Chemical Industry Co., Ltd. PTFE flat sheets were collected from Taobao (China) Software Co. , Ltd. Au sensor (QSX301) for QCM-D test was purchased from Biolin Scientific (Sweden). Unless state otherwise, deionized water (DI, ≥18 MΩ cm) with total organic carbon (TOC) concentration of lower than 3 ppb was collected from a water purification system (Milli-Q® IQ). All the chemicals and materials in this work were used as received.

1.2. Membrane fabrication

ANF dispersion preparation method can be found elsewhere[1]. Briefly, a 2% w v^{-1} ANF dispersion was prepared by dispersing Kevlar pulps with potassium hydroxide solution in dimethyl sulfoxide using mechanical stirring at room temperature and hermetic environment for 2 weeks.

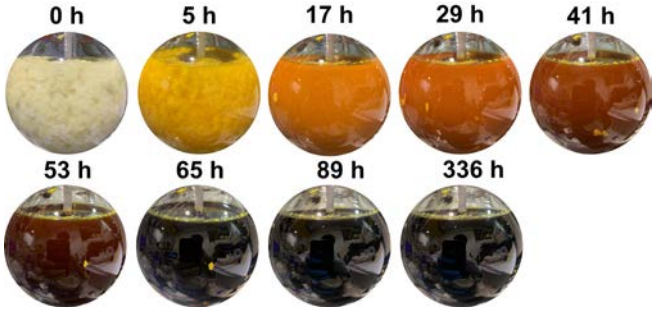

Fig. S1 Photographs of the preparation process for the ANF dispersion.

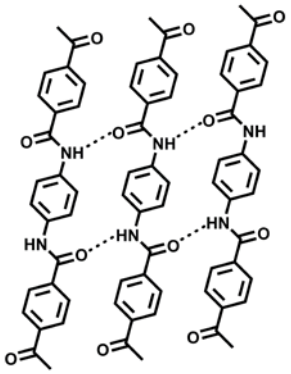

Fig. S2 Chemical structure for the Kevlar.

The conventional interfacial polymerization (IP) process was performed by pouring a hexane solution of TMC onto an aqueous solution of amine impregnated substrate for 1 minute. In this study, we conducted this process with a DCM solution of TMC atop a PIP impregnated solvent-resistance substrate (ANF hydrogel).

To study the effect of PIP concentration on the synthesized polyamide (PA), TMC was kept constant at 0.5% w v^{-1}, and the concentrations of PIP were varied at 0.01, 0.02,

0.03, 0.04, 0.05, and 0.06% w v^{-1}. The corresponding membranes are denoted as T5P1, T5P2, T5P3, T5P4, T5P5 and T5P6 respectively.

To study the effect of solvent activation on these prepared membranes, further activation process was performed by soaking PA membranes in DCM overnight. The corresponding activated membranes are denoted as AcT5P1, AcT5P2, AcT5P3, AcT5P4, AcT5P5 and AcT5P6.

To study the effect of TMC concentration on PA structure and performance, we fixed the optimized concentration of PIP (0.04% w v^{-1}), and the concentration of TMC used for IP reaction are 0.1, 0.2, 0.3, 0.4, and 0.6% w v^{-1}. The corresponding membranes are denoted as T1P4, T2P4, T3P4, T4P4, and T6P4.

The control IP process was performed by pouring a hexane solution of TMC (0.5% w v^{-1}) onto an ANF hydrogel with PIP solution (0.04% w v^{-1}) for 1 minute. The corresponding membrane was denoted as H-T5P4.

Furthermore, to study the effect of substrate on PA structure and performance, we carried out the IP process atop a solvent-resistant polyacrylonitrile (PAN) substrate. Specifically, the membrane was prepared by using a hexane/DCM solution of TMC (0.5% w v^{-1}) and a PIP solution (1% w v^{-1}) impregnated PAN substrate for IP reaction. The corresponding TFC PA membranes were named as H-T5P100@PAN and T5P100@PAN respectively.

All prepared TFC membranes were stored in DI water at 4 ℃ before use.

1.3. Characterization methods

The SEM images of the surface, rear, and cross-section of samples were collected by a high-resolution field emission scanning electron microscopy (Hitachi S-4800, FEG, UK) with a 5 keV of operating voltage. The surface texture of the PA rejection layer including height, phase and Young's modulus was mapped out by AFM (Bruker Dimension ICON, Multimode 8, MA) based on tapping mode. The cross-sectional TEM image of ultrathin specimens was observed through the Philips CM100 TEM (Netherlands) with a 100 keV of accelerating voltage. The surface and cross-sectional morphology of a hydrated TFC membrane fabricated with DCM were scanned using CryoSEM (FEI Quanta 450, Thermo Fisher Scientific Inc., USA). The elemental composition of the top PA rejection layer was analyzed through an X-ray photoelectron spectroscopy (Thermo Scientific NEXSA, Thermo Fisher Scientific, US) under a constant mono Al Kα source (1486.6 eV), a 15 keV of accelerating voltage and a 15 mA of current. The concentration of monomers in solvents was determined by a model UH5300 UV-Vis spectrophotometer. The streaming potential of the PA surface layer was measured using an electrokinetic analyzer (SurPASS^{TM} 3, Anton Paar GmbH, Austria-Europe). The PIP adsorption test was conducted using QCM-D. Typically, dispersions including ANF (2% w v^{-1}), PES (10% w v^{-1}) and PAN (5% w v^{-1}) were spin-coated atop the Au sensor with a speed of 12000 rpm lasting for 30 s. The loading amount of vacuum-dried coating was obtained when the system reaches equilibrium. During adsorption process, DI was firstly pumped into the module with a speed of 80 μL min^{-1}. After 3 h for equilibrium, 0.04% w v^{-1} PIP/DI solution was drawn to the

module with constant flow speed. The change of frequency and dispassion shift was then recorded. The adsorption mass can be calculated based on Sauerbrey equation[2]:

$$\frac{\Delta m}{S_A} = -\frac{C\Delta f_n}{n} \quad (1)$$

where Δm (g) and S_A (cm^2) is the sensor mass change and active surface area, C (g cm^{-2} Hz^{-1}), Δf_n (Hz) and n is the Sauerbrey constant, the change of resonance frequency shift, and the harmonic overtone order, respectively.

PADBES measurements based on positron annihilation were carried out with ^{22}Na source and the annihilation γ rays were recorded with Ge detector. Specifically, a regulated bias (0.18-5.18 keV) was applied to achieve the acceleration of the slow positrons, then these mono-energetic positrons were magnetically guided to the sample chamber and annihilated with the electrons of the PA rejection layer. After the pick-off quenching of positrons in the free volume, the yielded *S* parameter, which was determined as the ratio of the counts of γ rays range from 510.2 to 511.8 keV to the total counts of γ rays range from 499.5 to 522.5 keV, was obtained to reflect the depth profile of free volume in PA rejection layer.

The salts separation was performed in pressurized membrane cells with an active filtration area of 2 cm^2 (rectangular shape, 1 cm × 2 cm). Membrane coupons were mounted into the cells followed by pre-compaction with a feed solution (salts solution or DI water) for 1 hour before the collection of permeate. The recirculated feed solution contains 1 g L^{-1} salt (Na_2SO_4, $MgSO_4$, NaCl, or $MgCl_2$) for salts rejection measurements

160 or DI water for pure water permeance evaluation. The measurement was conducted with
161 a constant cross-flow velocity of 24 L h^{-1} and an applied pressure of 5 bar.

162 The salt rejection, R (%), was defined as the following equation:

$$R = (1-\frac{C_p}{C_f})\times 100\% \quad (2)$$

163 where C_f and C_p are the conductivity, measured by a conductivity meter (Ultrameter II,
164 Myron L Company, Carlsbad, CA), of the feed and permeate, respectively.

165 The water permeance, determined by the water volume collected over a period, was
166 calculated by:

$$A = \frac{\Delta V}{S \times \Delta t \times \Delta P} \quad (3)$$

167 where A (L m^{-2} h^{-1} bar^{-1}), ΔV (L), S (m^2), Δt (h) is the pure water permeance, the water
168 volume collected, active filtration area, collection time, and the applied pressure,
169 respectively.

170 The membrane pore size distribution was evaluated based on the rejection of organic
171 model solutes, which is performed using the cells same with those for salts separation.
172 Specifically, model solutes of glycerol, glucose, sucrose, and dextran (~1000 Da) with
173 the same concentration at 0.2 g L^{-1} were used to measure the rejection of solutes for
174 membranes, as determined by the concentration of feed and permeate solutions using
175 the total organic carbon (TOC) with a TOC analyzer (TOC-$L_{CPH/CPN}^{TM}$, Shimadzu
176 Corporation, Japan). The molecular weight cut-off (MWCO) of PA active layer was
177 defined according to the molecular weight value with TOC rejection reaching 90%. The

pore size distribution of PA active layer can be expressed using the probability density function (PDF) (1):

$$\frac{dR(r_p)}{dr_p} = \frac{1}{r_p \ln \sigma_p \sqrt{2\pi}} \exp\left[\frac{(\ln r_p - \ln \mu_p)^2}{2(\ln \sigma_p)^2}\right] \quad (2)$$

where $R(r_p)$ and r_p represent the active layer's TOC rejection and Stokes radii of the model solutes respectively. The mean pore radius μ_p of PA active layer was assumed to equal the Stokes radius of model solute with TOC rejection of 50%. σ_p is the geometric standard deviation, which was acquired from the ratio of Stokes radii when TOC rejection equals 84.13% to that equal 50%.

The Stokes radii of glycerol, glucose, sucrose was calculated based on the following equation[3]:

$$\log_{10} r_p = -1.4962 + 0.4654 \log_{10} M \quad (3)$$

where M is the corresponding MW of solutes.

For dextran (MW~1000 Da)[4],

$$r_p = 0.33 \times (M)^{0.46} \quad (4)$$

The PA membrane ionized carboxyl group density under various pH conditions can be quantified by the content of bonded silver ions. As reported[5], tailored samples (rectangular shape, 1 cm × 2 cm) were soaked in silver nitrate solution (10 mL, 40 μM L^{-1}) twice at a specific pH for 10 min. Unbounded ions were removed by rinsing the membrane 4 times using silver nitrate solution (10 mL, 1 μM L^{-1}) at the same pH for 7 min. After that, the bonded silver ions were eluted by immersion of membrane in nitric

acid solution (5 mL, 1% w v^{-1}) for 30 min. Finally, the silver ion concentration of the eluent was measured to determine the contents of carboxyl groups by inductively coupled plasma mass spectrometry (ICP-MS, Agilent 7900). The ionized carboxyl group density can be determined by the following equation.

$$[R\text{-}COO^-]=\frac{C_{Ag^+}\times V_{Ag^+}\times N_A}{S_m} \quad (5)$$

where $[R\text{-}COO^-]$ (sites nm^{-2}), C_{Ag+} (mol L^{-1}), V_{Ag+} (L), and N_A (6.02×10^{23} mol^{-1}), is ionized carboxyl group density, the silver concentration, the volume of eluate, and the Avogadro's number, respectively. S_m (nm^{-2}) is the active surface area of samples with the same size and shape of those for filtration test.

2. PIP diffusion process

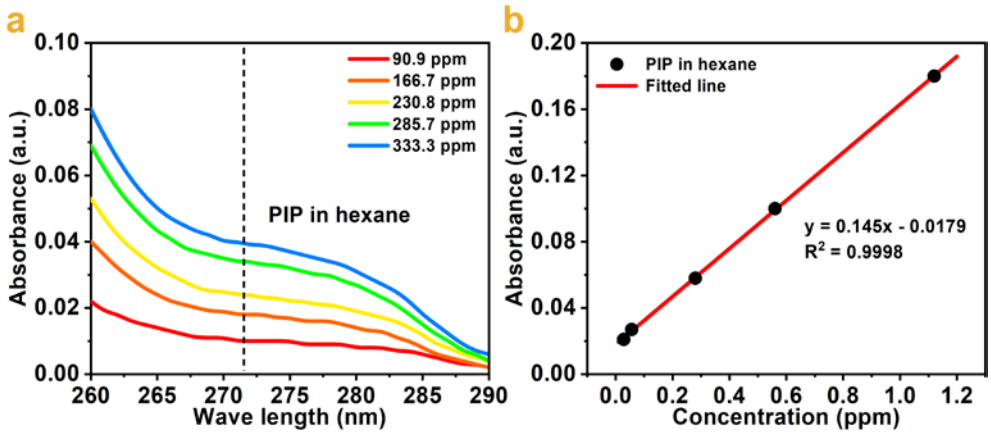

Fig. S3 Ultraviolet-visible (UV-Vis) spectra of PIP in hexane. (**a**) UV-Vis absorbance of PIP in hexane. (**b**) Calibration curve of absorbance as a function of monomers concentration.

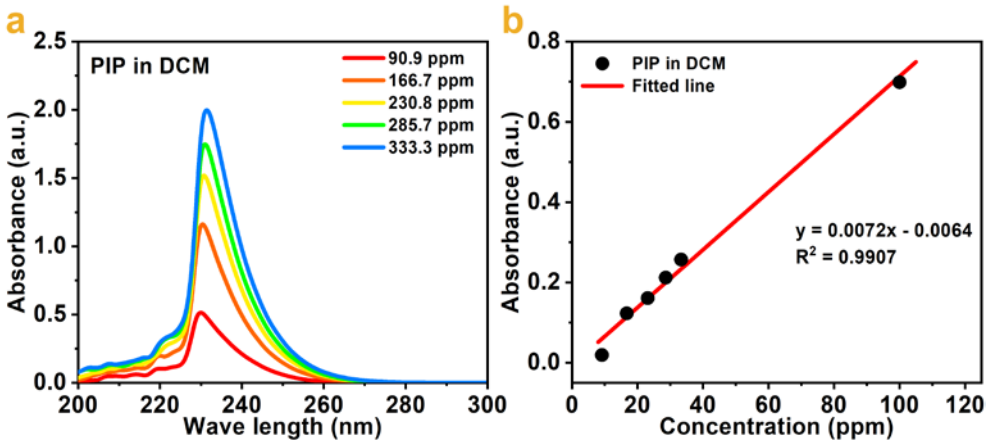

208

209 **Fig. S4 UV-Vis spectra of PIP in DCM.** (**a**) UV-Vis absorbance of PIP in DCM. (**b**)

210 Calibration curve of absorbance as a function of monomers concentration.

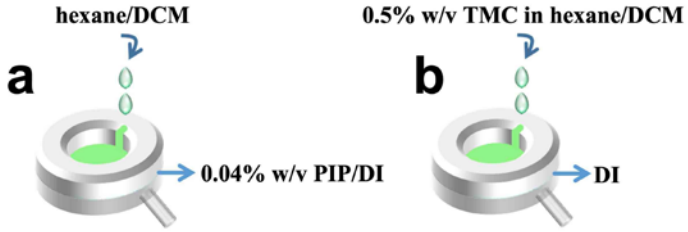

211

212 **Fig. S5 1 min diffusion set up.** (**a**) PIP diffuses from aqueous phase to organic phase.

213 (**b**) TMC diffuses from organic phase to aqueous phase.

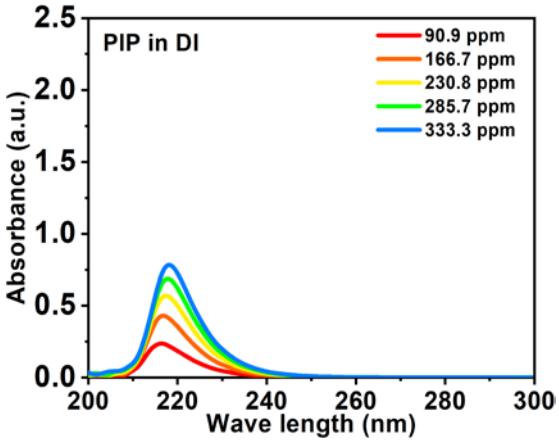

214

215 **Fig. S6 UV-Vis spectra of PIP in DI.**

3. Morphology and structure

3.1. The effect of monomer concentration and substrate on membrane morphology

3.1.1. Surface and cross-sectional cryoSEM images of membrane prepared with DCM

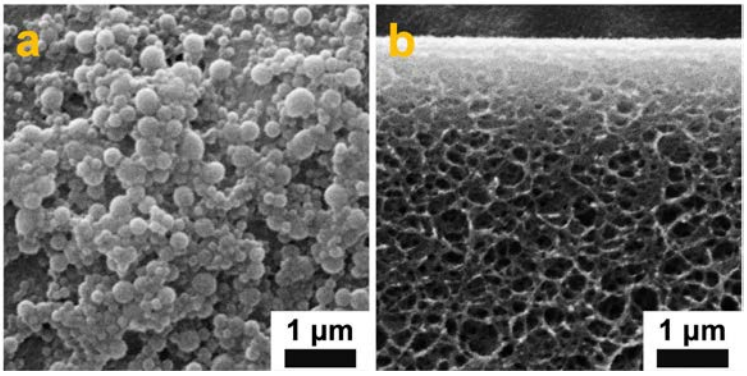

Fig. S7 Cryo-SEM images of the surface and cross section of PA active layer prepared with DCM. (**a**) surface image of PA prepared with DCM. (**b**) cross-sectional image of PA prepared with DCM. The corresponding TMC and PIP concentrations used for the IP reaction are 0.5% w v^{-1} and 0.04% w v^{-1}, respectively. To unambiguously unravel the real morphology of hydrogel-supported PA membrane in an aqueous state, the surface and cross-section of hydrated TFC membranes were scanned using CryoSEM (FEI Quanta 450, Thermo Fisher Scientific Inc., USA). Before observation of the sample surface, hydrated samples were frozen using a liquid nitrogen slush bath. Frozen samples were kept in vacuum condition sublimating for 5 min at -90 ℃ and then the sputter coating with gold was carried out at the same condition for 60 seconds with an operating current of 10 mA. During the preparation process, samples should be kept in a vacuum and cryo environment to prevent the formation of ice crystals. For the cross-sectional CryoSEM image, the fracturing process was conducted after using

liquid nitrogen slush. The observation for membrane surface or cross-section was finally performed at -140 ℃ with an accelerating voltage of 10 keV.

3.1.2. Surface SEM images of membranes prepared with DCM

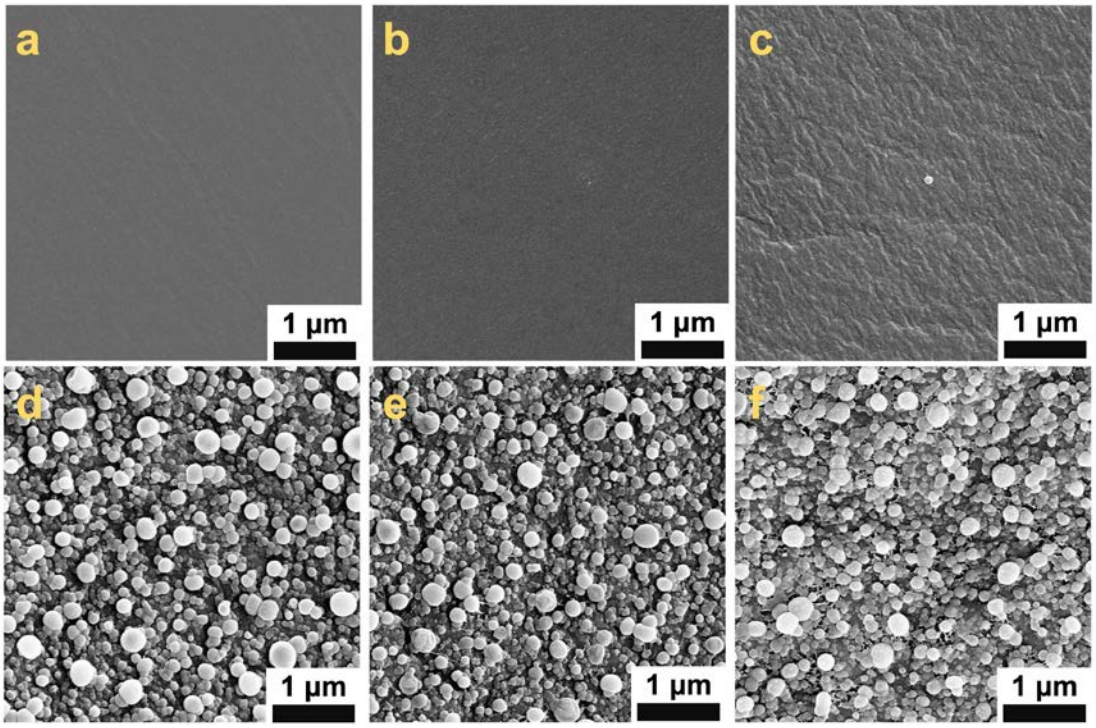

Fig. S8 Surface SEM images of PA active layer prepared with a constant TMC concentration (0.5% w v^{-1}) and varying PIP concentrations. (**a**) 0.01% w v^{-1} PIP. (**b**) 0.02% w v^{-1} PIP. (**c**) 0.03% w v^{-1} PIP. (**d**) 0.04% w v^{-1} PIP. (**e**) 0.05% w v^{-1} PIP. (**f**) 0.06% w v^{-1} PIP.

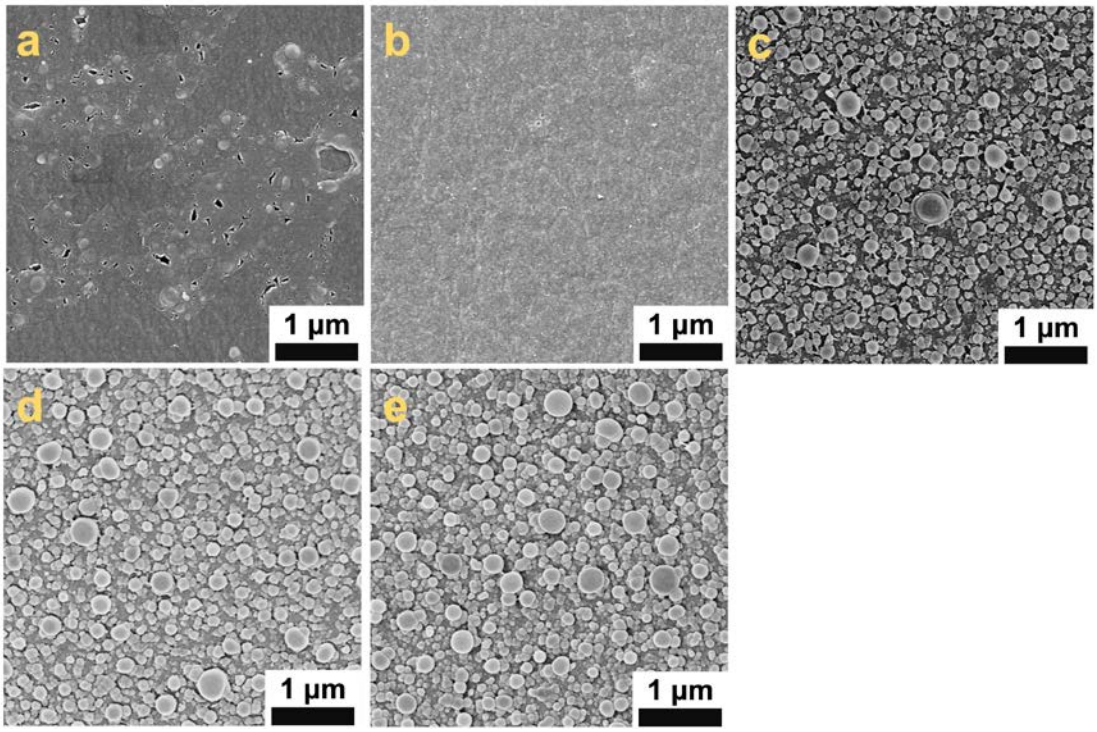

Fig. S9 Surface SEM images of activated PA layer prepared with a constant TMC concentration (0.5% w v^{-1}) and varying PIP concentrations. (a-f) The PIP concentrations vary from 0.02% w v^{-1} (**a**), 0.03% w v^{-1} PIP (**b**), 0.04% w v^{-1} PIP (**c**), 0.05% w v^{-1} PIP (**d**), and 0.06% w v^{-1} PIP (**e**). The activation process was performed by soaking PA membranes in DCM overnight.

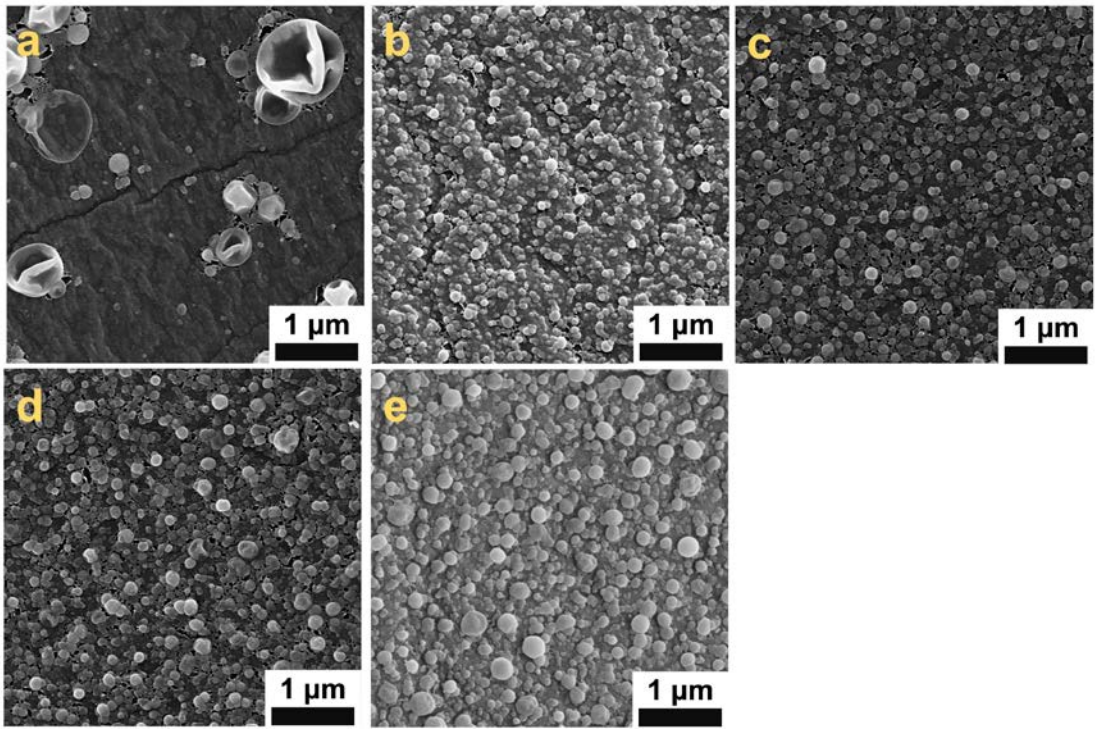

Fig. S10 Surface SEM images of PA active layer prepared with a constant PIP concentration (0.04% w v^{-1}) and varying TMC concentrations. (**a**) 0.1% w v^{-1} TMC. (**b**) 0.2% w v^{-1} TMC. (**c**) 0.3% w v^{-1} TMC. (**d**) 0.4% w v^{-1} TMC. (**e**) 0.6% w v^{-1} TMC.

3.1.3. Cross-sectional SEM images

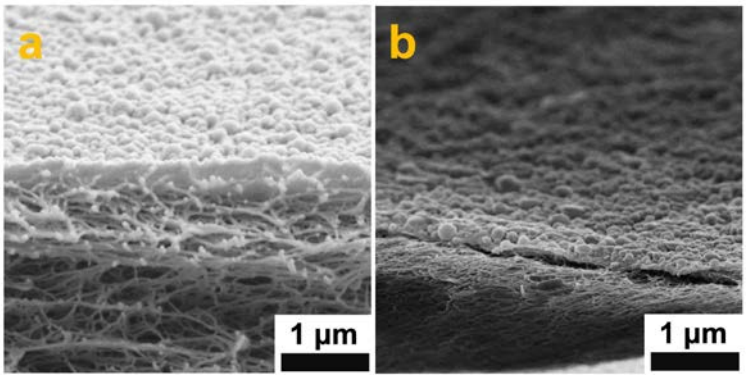

Fig. S11 Cross-sectional SEM images of PA rejection layer prepared with DCM and subsequent solvent activation. (**a**) PA prepared with DCM. (**b**) PA prepared with DCM and subsequent activation. The corresponding TMC and PIP concentrations used

for the IP reaction are 0.5% w v^{-1} and 0.04% w v^{-1}, respectively. The activation process was performed by soaking PA membranes in DCM overnight.

3.1.4. Cross-sectional TEM images

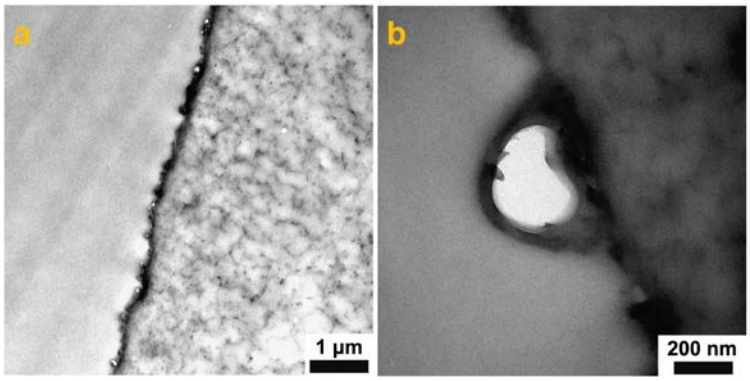

Fig. S12 Low-magnification and high-magnification cross-sectional TEM images of PA active layer prepared with DCM. (**a**) Low magnification. (**b**) High magnification. The corresponding TMC and PIP concentrations used for the IP reaction are 0.5% w v^{-1} and 0.04% w v^{-1}, respectively.

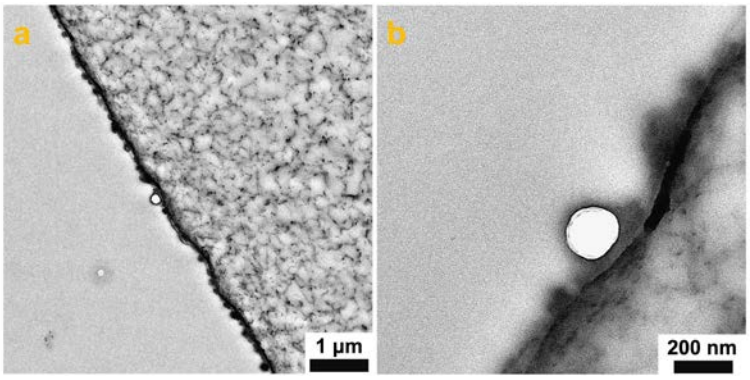

Fig. S13 Low-magnification and high-magnification cross-sectional TEM images of PA active layer prepared with DCM. (**a**) Low magnification. (**b**) High magnification. The corresponding TMC and PIP concentrations used for the IP reaction are 0.2% w v^{-1} and 0.04% w v^{-1}, respectively.

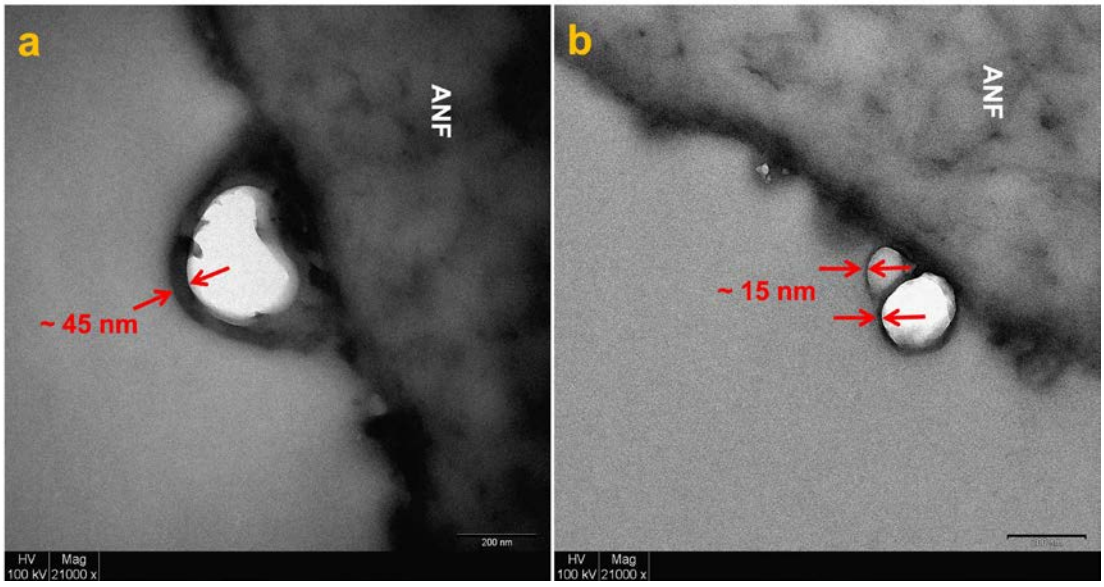

Fig. S14 High-magnification cross-sectional TEM images of PA active layer prepared with DCM and subsequent solvent activation. (**a**) PA prepared with DCM. (**b**) PA prepared with DCM and subsequent activation. The corresponding TMC and PIP concentrations used for the IP reaction are 0.5% w v^{-1} and 0.04% w v^{-1}, respectively.

3.1.5. SEM images of the TFC PA membranes atop PAN substrate

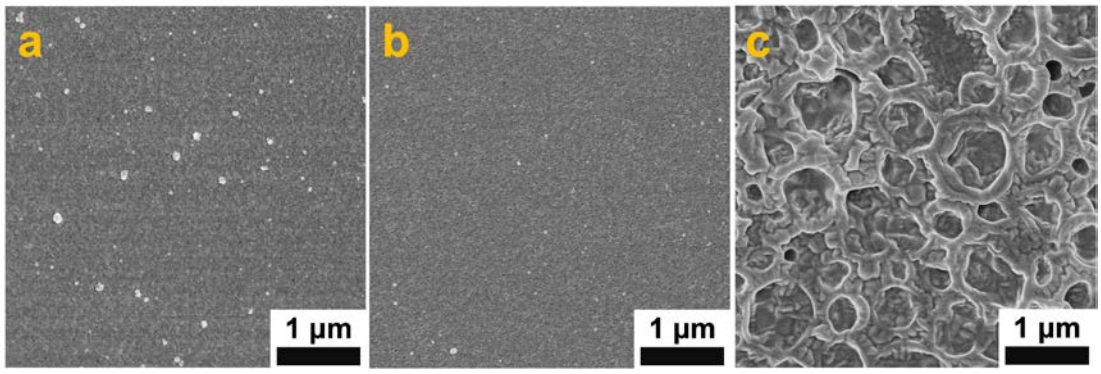

Fig. S15 Surface SEM images of the PA membranes prepared with hexane and DCM atop commercial PAN substrate. (**a**) Surface SEM image of PA active layer prepared with hexane. (**b**) Surface SEM image of PA active layer prepared with DCM. (**c**) Surface SEM images of the commercial PAN substrate. Specifically, the PAN substrate was first wetted with PIP/DI solution. After rolling out the excess solution,

the IP reaction will occur on the substrate surface when pouring a TMC/hexane or TMC/DCM (0.5% w v^{-1}) solution, yielding the polyamide membranes. Due to the hydrophobicity of the PAN substrate, an increased concentration of PIP/DI solution (1% w v^{-1}) was conducted with a longer wetting time (10 min) to obtain the TFC PA membranes for this study.

3.2. XPS results

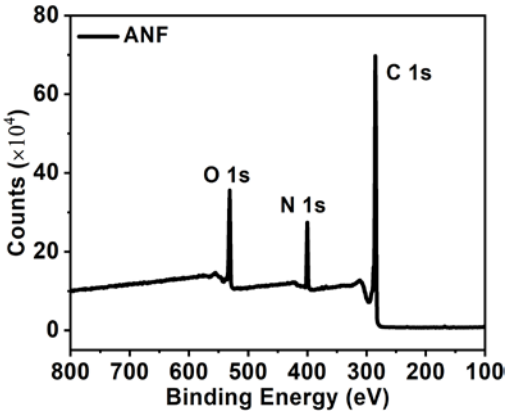

Fig. S16 Top surface XPS spectrum of ANF substrate.

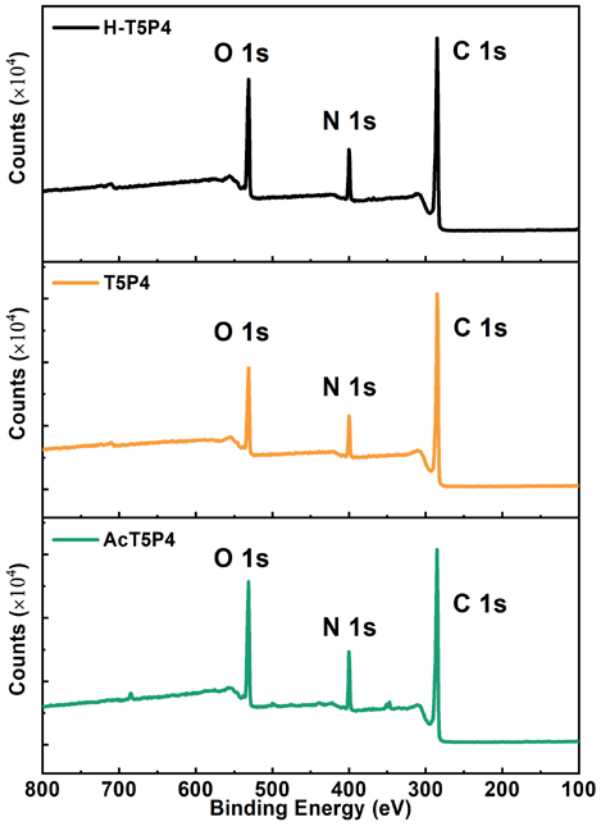

Fig. S17 Top surface XPS spectrum of PA active layer prepared with hexane, DCM and subsequent solvent activation. The black curve represents PA prepared with hexane, the orange curve represents PA prepared with DCM and the dark cyan curve represents PA prepared with DCM and subsequent activation. The corresponding TMC and PIP concentrations used for the IP reaction are 0.5% w v^{-1} and 0.04% w v^{-1}, respectively.

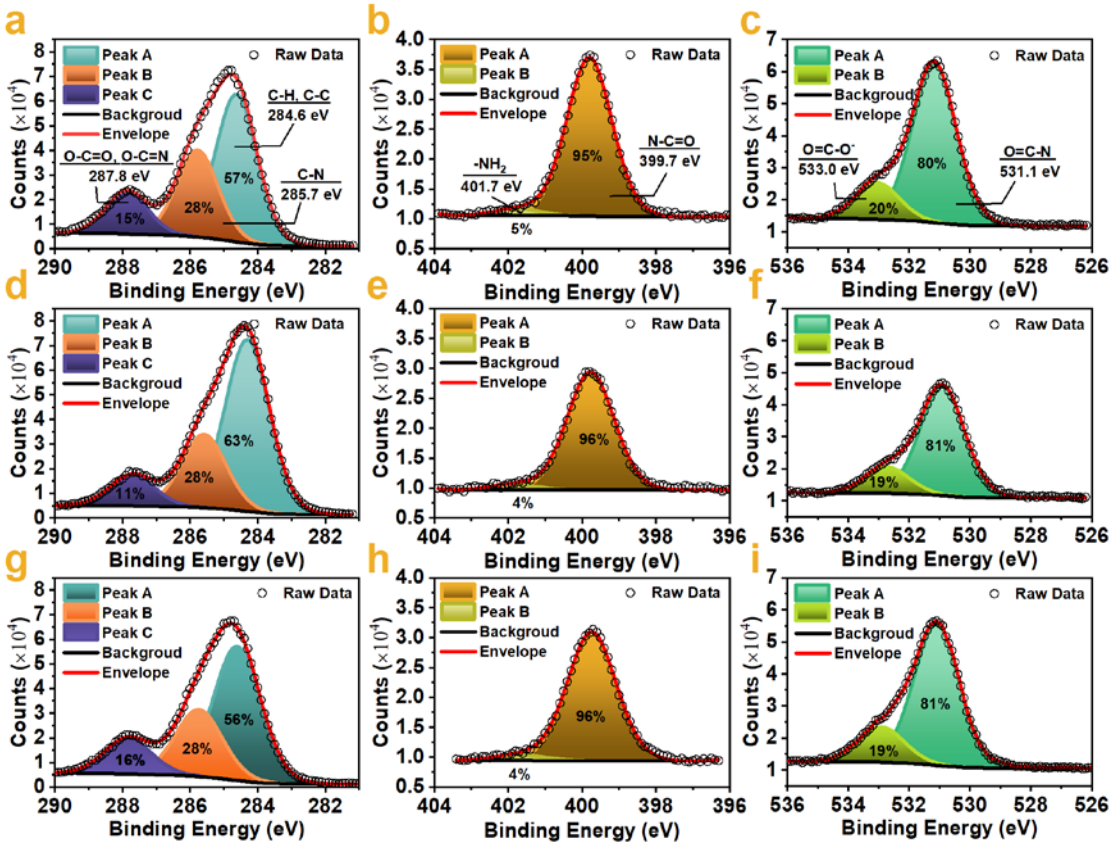

Fig. S18 Top surface high-resolution XPS C 1s, N 1s and O 1s spectra of PA active layer prepared with hexane, DCM and subsequent solvent activation. (**a, b, c**) PA prepared with hexane. (**d, e, f**) PA prepared with DCM. (**g, h, i**) PA prepared with DCM and subsequent activation. The corresponding TMC and PIP concentrations used for the IP reaction are 0.5% w v^{-1} and 0.04% w v^{-1}, respectively.

Table S1 Surface O/N ratio of PA and ANF membranes.

PA membranes*				
Organic solvent for IP	**TMC Content (% w v^{-1})**	**PIP Content (% w v^{-1})**	**Solvent activation**	**O/N ratio**
hexane	0.5	0.04	/	1.83 ± 0.07
DCM	0.5	0.04	/	1.56 ± 0.09
DCM	0.5	0.04	DCM	1.76 ± 0.10

Note*: The surface O/N ratio of ANF substrate is 1.08 ± 0.01.

3.3. Young's modulus of membrane surface

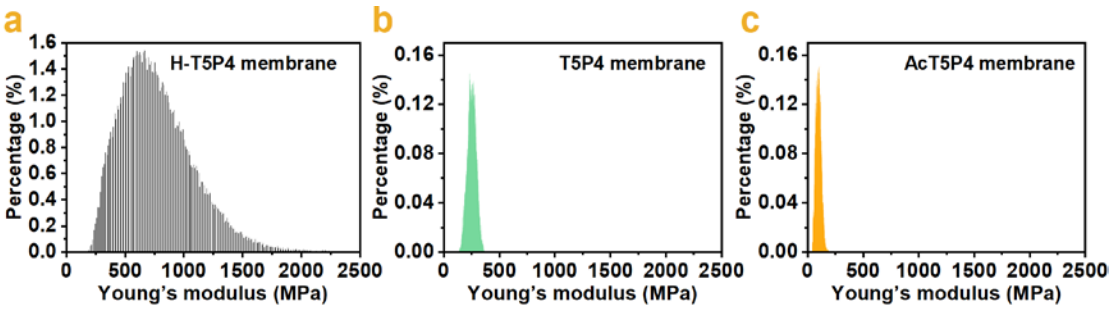

Fig. S19 Young's modulus distribution of PA active layer prepared with hexane, DCM and subsequent solvent activation. (**a**) PA prepared with hexane. (**b**) PA prepared with DCM. (**c**) PA prepared with DCM and subsequent activation. The corresponding TMC and PIP concentrations used for the IP reaction are 0.5% w v^{-1} and 0.04% w v^{-1}, respectively.

3.4. The effective pore size and its distribution of membrane

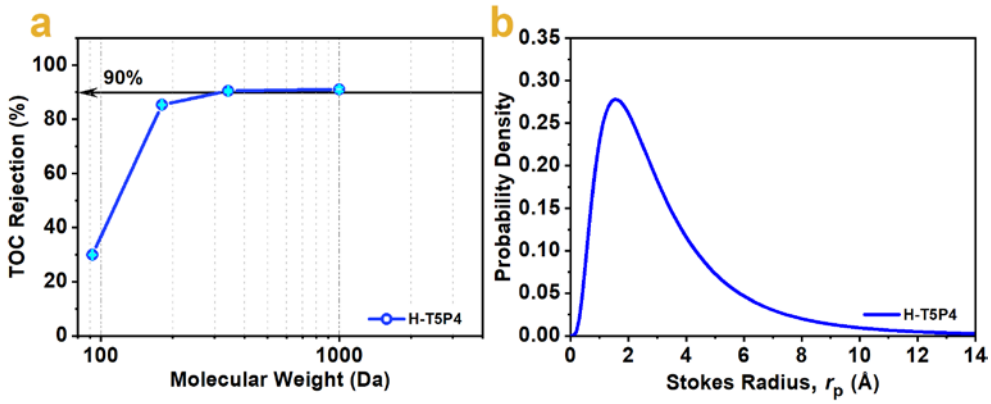

Fig. S20 MWCO and PDF of PA membrane prepared with hexane. (a) Rejection of neutral solutes. (**b)** Pore size distribution of the membrane estimated with data presented in (**a**) based on Supplementary Equation 1. The corresponding TMC and PIP concentrations used for the IP reaction are 0.5% w v^{-1} and 0.04% w v^{-1}, respectively.

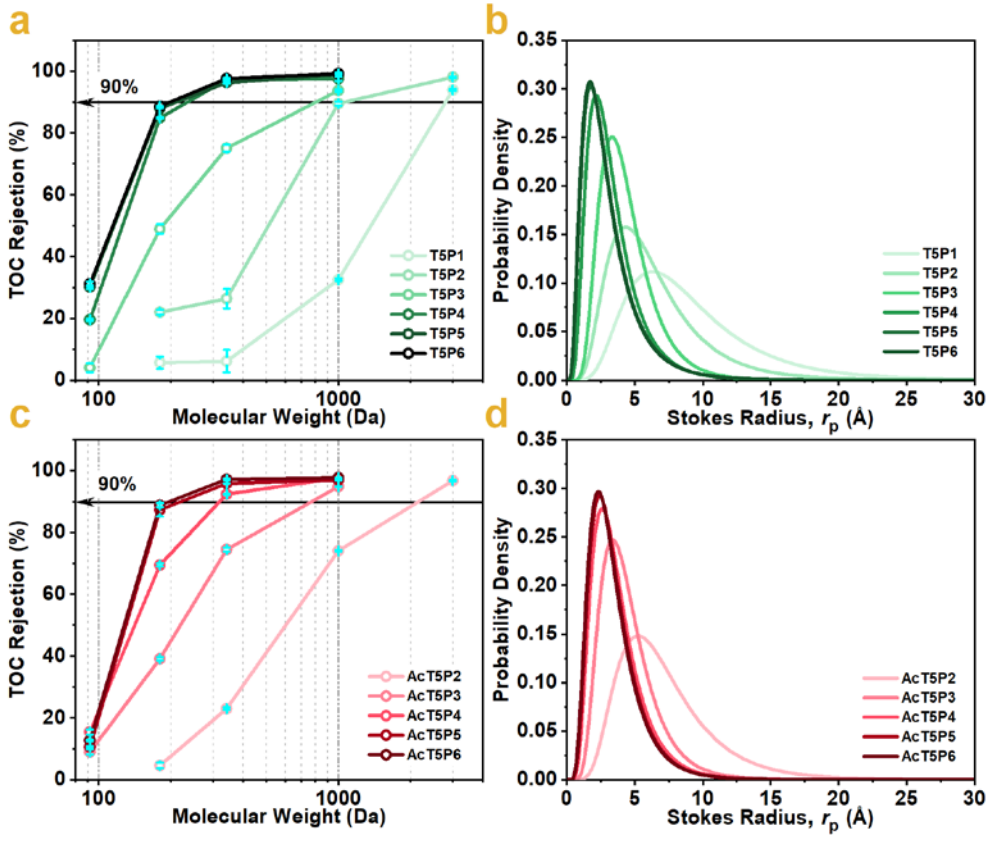

Fig. S21 MWCO and PDF of PA membranes prepared with DCM and subsequent solvent activation. (**a, c)** TOC rejection of neutral solutes. (**b, d)** Pore size distribution

of the membranes estimated with data presented in (**a, c**) based on Supplementary Equation 1. (**a, b**) The PA active layer was prepared with a constant TMC concentration (0.5% w v^{-1}) and the concentrations of PIP were varied at 0.01, 0.02, 0.03, 0.04, 0.05, and 0.06% w v^{-1}. (**c, d**) The activated PA membranes was prepared with a constant TMC concentration (0.5% w v^{-1}) and the concentrations of PIP were varied at 0.02, 0.03, 0.04, 0.05, and 0.06% w v^{-1}.

328 **Table S2** The effective mean pore radius μ_p, geometric standard deviation σ_p and

329 molecular weight cut-off (MWCO) of ANF-supported TFC membranes.

PA membranes						
Organic solvent for IP	**TMC Content (% w v^{-1})**	**PIP Content (% w v^{-1})**	**Solvent activation**	**μ_p (Å)**	**σ_p**	**MWCO (Da)**
hexane	0.5	0.04	/	2.591	2.042	311
DCM	0.5	0.01	/	8.081	1.651	2822
DCM	0.5	0.02	/	5.628	1.671	1099
DCM	0.5	0.03	/	4.013	1.547	815
DCM	0.5	0.04	/	2.893	1.726	234
DCM	0.5	0.05	/	2.568	1.863	213
DCM	0.5	0.06	/	2.517	1.873	204
DCM	0.5	0.02	DCM	6.475	1.589	2183
DCM	0.5	0.03	DCM	4.069	1.548	781
DCM	0.5	0.04	DCM	3.285	1.634	319
DCM	0.5	0.05	DCM	3.082	1.652	221
DCM	0.5	0.06	DCM	2.999	1.667	203

330

3.5 Surface AFM topography

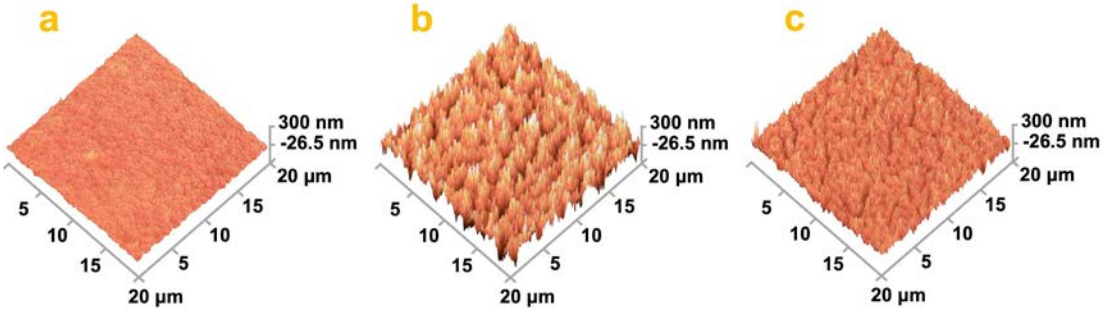

Fig. S22 AFM topography of PA active layer prepared with hexane, DCM and subsequent solvent activation. (**a**) PA prepared with hexane. (**b**) PA prepared with DCM. (**c**) PA prepared with DCM and subsequent activation. The corresponding TMC and PIP concentrations used for the IP reaction are 0.5% w v^{-1} and 0.04% w v^{-1}, respectively.

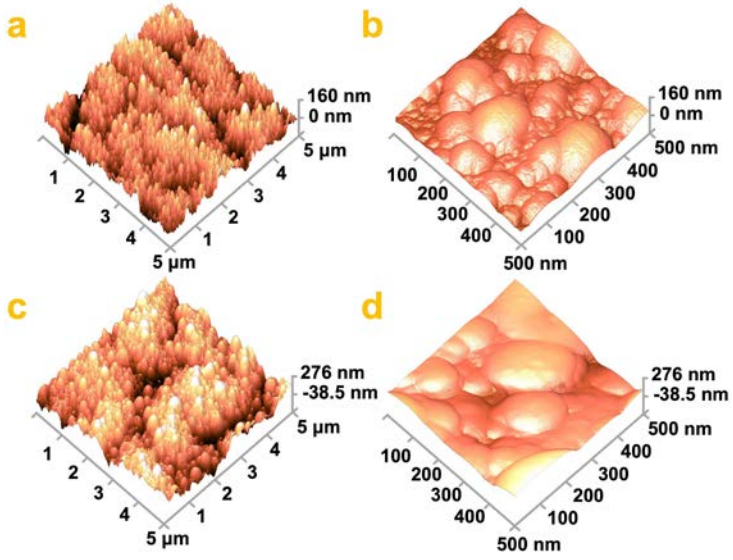

Fig. S23 Low-magnification and high-magnification surface AFM height images of PA active layer prepared with DCM and subsequent solvent activation. (**a, b**) PA prepared with DCM. (**c, d**) PA prepared with DCM and subsequent activation. The

corresponding TMC and PIP concentrations used for the IP reaction are 0.5% w v^{-1} and 0.04% w v^{-1}, respectively.

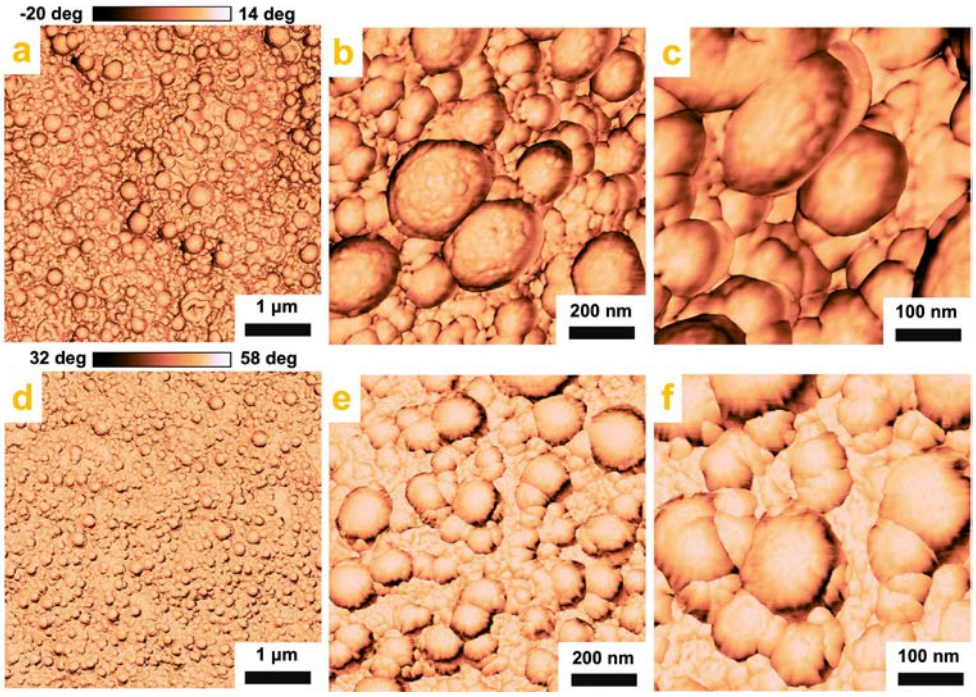

Fig. S24 Surface AFM phase images of PA active layer prepared with DCM and subsequent solvent activation. (**a, b, c**) PA prepared with DCM. (**d, e, f**) PA prepared with DCM and subsequent activation. The corresponding TMC and PIP concentrations used for the IP reaction are 0.5% w v^{-1} and 0.04% w v^{-1}, respectively.

4. Separation performance and structure

4.1. Salts separation

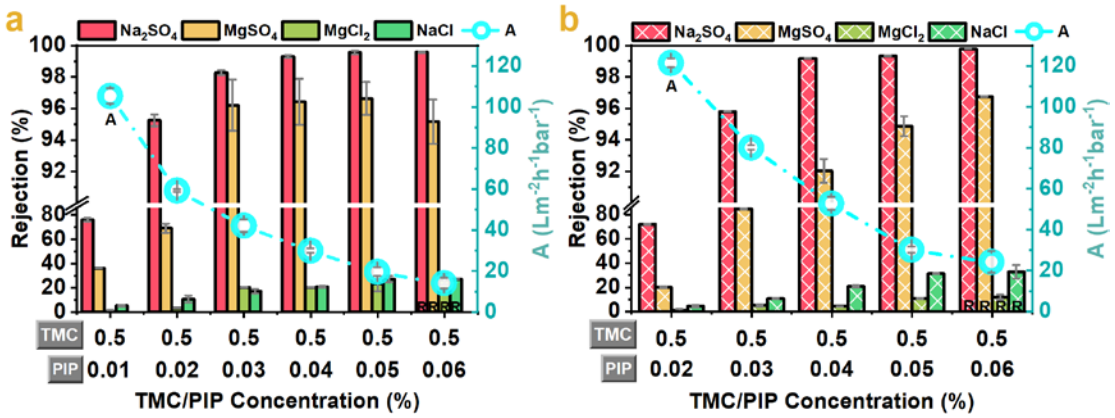

Fig. S25 Separation performance of PA membranes prepared with DCM and subsequent solvent activation. (**a**) The PA active layer was prepared with a constant TMC concentration (0.5% w v^{-1}) and the concentrations of PIP were varied at 0.01, 0.02, 0.03, 0.04, 0.05, and 0.06% w v^{-1}. (**b**) The activated PA membranes was prepared with a constant TMC concentration (0.5% w v^{-1}) and the concentrations of PIP were varied at 0.02, 0.03, 0.04, 0.05, and 0.06% w v^{-1}.

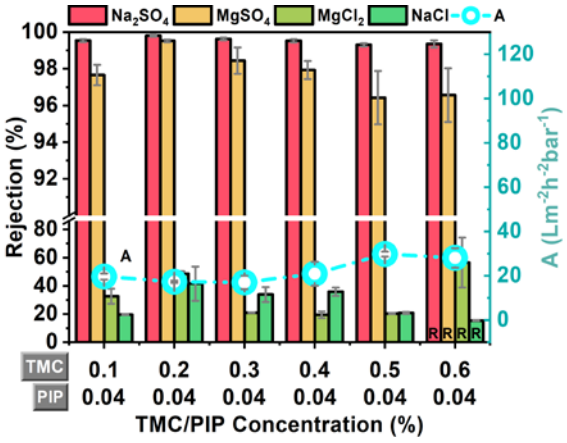

Fig. S26 Separation performance of PA membranes prepared with DCM. The PA active layer was prepared with a constant PIP concentration (0.04% w v^{-1}) and the concentrations of TMC were varied at 0.1, 0.2, 0.3, 0.4, 0.5 and 0.6% w v^{-1}.

4.2. The effective pore size, pore size distribution and MWCO of TFC PA membranes based on PAN substrate

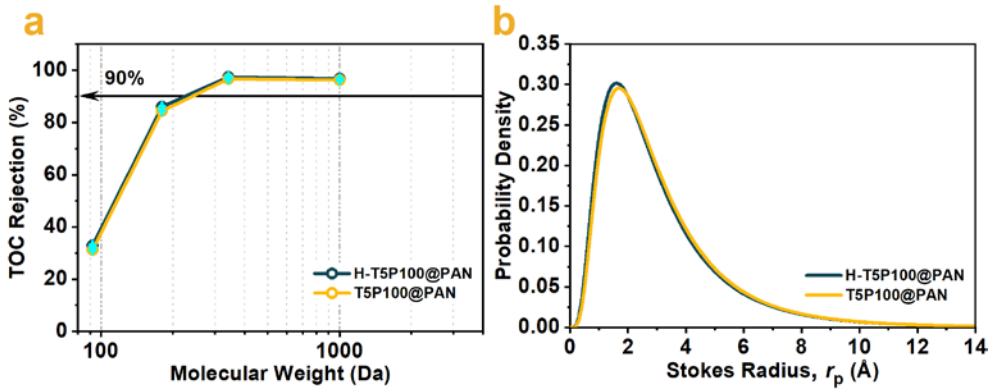

Fig. S27 MWCO and PDF of PA membranes prepared atop PAN substrate. (a) Rejection of neutral solutes. (**b)** Pore size distribution of the TFC-PA membranes estimated with data presented in (**a**) based on Supplementary Equation 1. The dark blue curve represents PA prepared with hexane and the yellow curve represents PA prepared with DCM. The corresponding TMC and PIP concentrations used for the IP reaction are 0.5% w v^{-1} and 1% w v^{-1}, respectively.

Table S3 The mean pore radius μ_p, geometric standard deviation σ_p and MWCO of TFC PA membranes based on commercial PAN substrate.

PA Membranes					
Organic solvent for IP	**TMC Content (% w v^{-1})**	**PIP Content (% w v^{-1})**	**μ_p (Å)**	**σ_p**	**MWCO (Da)**
hexane	0.5	1.0	2.480	1.943	227
DCM	0.5	1.0	2.569	1.913	243

4.3. Ionized carboxyl group density of membranes and its Zeta potential

Table S4 Ionized carboxyl density under various solution pH with a unit of sites nm^{-2}.

PA membranes						
Organic solvent for IP	**TMC Content (% w v^{-1})**	**PIP Content (% w v^{-1})**	**Solvent activation**	**pH 3.5**	**pH 7**	**pH 10.5**
DCM	0.5	0.02	/	1.8 ± 0.1	51.9 ± 0.2	79.1 ± 0.1
DCM	0.5	0.04	/	1.8 ± 0.1	43.4 ± 0.3	70.5 ± 0.3
DCM	0.5	0.06	/	1.0 ± 0.1	33.6 ± 0.5	64.6 ± 0.8
DCM	0.5	0.02	DCM	2.0 ± 0.1	61. 6 ± 0.6	82.3 ± 2.1
DCM	0.5	0.04	DCM	1.8 ± 0.1	44.1 ± 0.2	73.5 ± 1.9
DCM	0.5	0.06	DCM	1.3 ± 0.1	39.0 ± 0.4	70.6 ± 1.0
hexane	0.5	0.04	/	1.8 ± 0.1	50.4 ± 0.2	121.9 ± 1.0

The membrane ionized carboxyl group density was quantified by the content of bonded silver ions under various pH conditions. Based on Supplementary Equation 4, The membrane ionized carboxyl group density can be estimated when the content of silver ion in the eluate was detected by ICP-MS. For ANF substrate, the ionized carboxyl group density at pH 3.5, pH 7 and pH 10.5 is 1.1 ± 0.2, 8.1 ± 0.6 and 30.5 ± 2.7 sites nm^{-2} respectively.

4.4. Long-term stability test

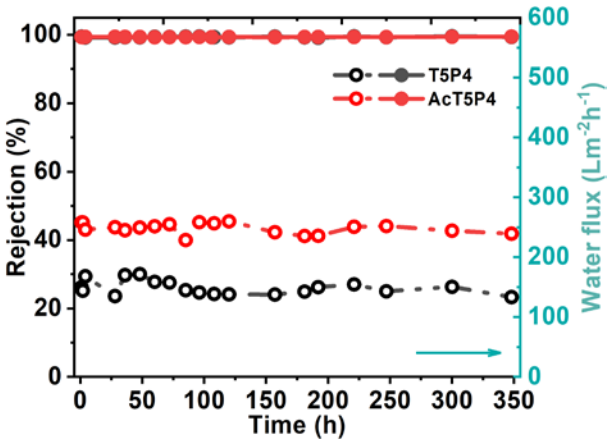

Fig. S28 Long-term stability test of PA membranes (~ 2 weeks) prepared with DCM and subsequent solvent activation. The corresponding TMC and PIP concentrations used for the IP reaction are 0.5% w v^{-1} and 0.04% w v^{-1}, respectively. The test conditions: 1000 ppm Na_2SO_4, 5 bar, room temperature and environmental pH.

4.5. Selected commercial nanofiltration membranes (NF90 and NF270)

The commercial NF90 and NF270 membranes were selected to conduct separation experiments based on the same parallel cells.

Table S5 The salts rejection, water permeance and selectivity for NF90 and NF270.

	NF90	**NF270**
R_{Na2SO4} (%)	99.5 ± 0.1	99.7 ± 0.1
R_{MgSO4} (%)	99.5 ± 0.1	99.5 ± 0.1
R_{MgCl2} (%)	96.1 ± 0.1	88.6 ± 0.1
R_{NaCl} (%)	67.8 ± 0.6	63.1 ± 0.4
Water permeance A (L m^{-2} h^{-1} bar^{-1})	7.4 ± 0.3	14.0 ± 0.2
A/B_{Na2SO4} (bar^{-1})	49.4	92.1
B_{NaCl}/B_{Na2SO4}	85.4	196.7

5. MD Details

5.1. H_2O, DCM, PIP, hexane, and Kevlar models

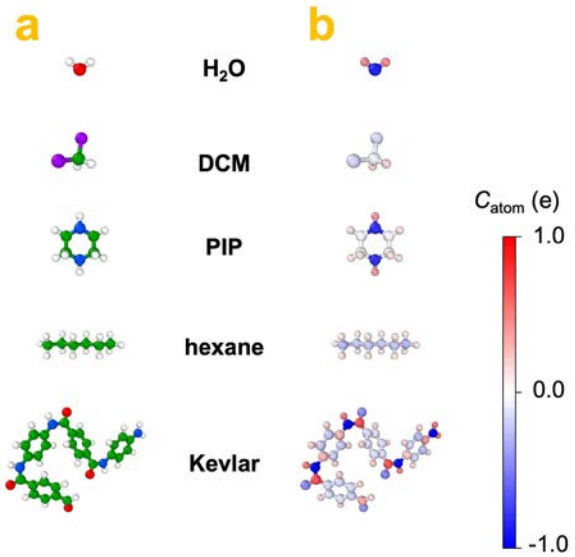

Fig. S29 Structural details of each component in molecular dynamics (MD) simulations. (**a**) The atomic structures of H_2O, DCM, PIP, hexane, and Kevlar (two repeated units), where white, red, blue, green, and purple colors represent H, O, N, C, and Cl atoms, respectively. (**b**) The atomic charge distributions (C_{atom}) of H_2O, DCM, PIP, hexane, and Kevlar.

5.2. Simulation details of self-diffusion process

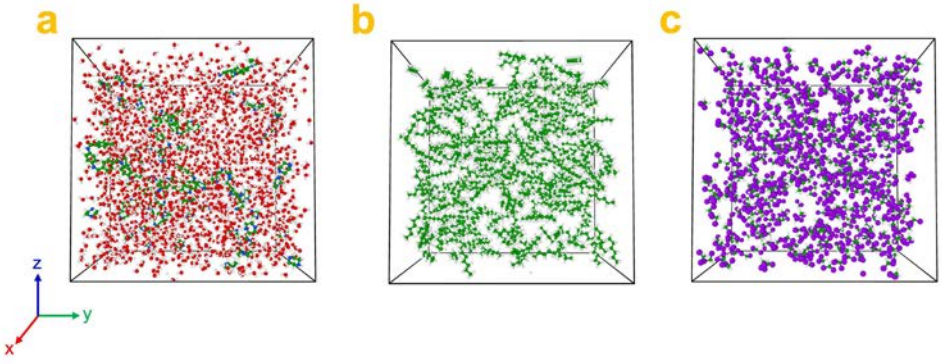

Fig. S30 The initial configurations of systems. (**a**) System ANF hydrogel (H_2O, Kevlar, and PIP). (**b**) System hexane. (**c**) System DCM.

406 Each bulk system including system ANF hydrogel, system hexane, and system DCM
407 was constructed to produce a reasonable initial density of each component. System ANF
408 hydrogel was built by combining PIP and Kevlar into the liquid bulk of H_2O, while
409 system hexane and DCM were built by hexane and DCM as the liquid bulk respectively.
410 Among these systems, a periodic boundary condition was applied with an initial size of
411 $6 \times 6 \times 6$ nm^3 for these systems to facilitate the following simulation process.

412 The diffusion process and the distribution of PIP were revealed by constructing
413 integrated systems with upper and lower regions (Fig. S28). System I was consisted of
414 system hexane (upper) and system ANF hydrogel (lower), and system II was consisted
415 of system DCM (upper) and system ANF hydrogel (lower). The number of each
416 component in the integrated systems were shown in Table S6.

417 **Table S6** The number of H_2O, DCM, PIP, hexane, and Kevlar in integrated systems.

Type	**H_2O**	**Kevlar**	**PIP**	**hexane**	**DCM**
System I	2128	8	48	296	/
System II	2128	8	48	/	600

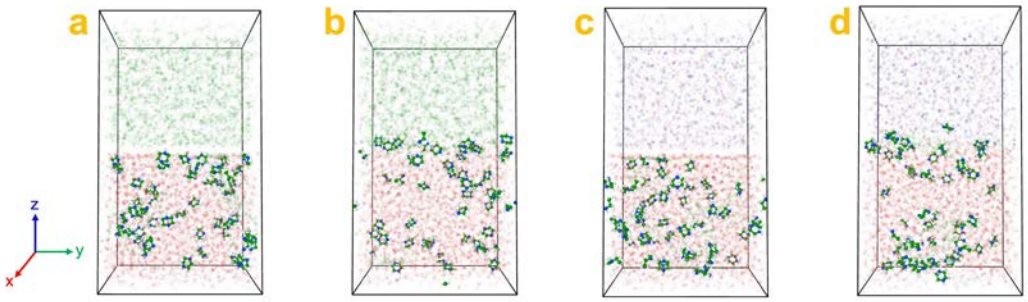

Fig. S31 MD simulation of the transport of PIP at the systems. The initial and equilibrium configurations of simulated integrated systems of system I (**a, b**) and system II (**c, d**).

The diffusion process and the distribution of PIP was examined by constructing system I (hexane as organic phase) and system II (DCM as organic phase). As shown in Fig. S29, both systems were consisted of upper and lower regions. The lower region of each system was built by combining PIP and Kevlar into the liquid bulk of H_2O. The upper region of each system was built by either hexane or DCM as the liquid bulk. Table S6 displays the number of H_2O, DCM, PIP, hexane, and Kevlar that are present in system I and II, respectively. To produce a more reasonable initial density in the upper and lower regions of system I and II, we first separated the upper and lower regions of system I and II into three separate individual bulk systems (see Fig. S28), which we designated as system ANF hydrogel, hexane, and DCM. For system ANF, hexane, and DCM, a periodic boundary condition (PBC) was applied in all three directions. The initial size of the PBC was set as $6 \times 6 \times 6$ nm^3. We used a computational software (PACKMOL)[6] to construct the initial configurations of all systems, and then all of the components were randomly introduced into the PBC (Fig. S28).

436 The extended simple point charge (SPC/E) model was used to describe H_2O,
437 which has been widely adopted since it predicts reasonable static and dynamic
438 propensities[7]. The parameters of the bond, angle, dihedral, van der Waals interactions,
439 and electrostatic interactions of PIP[8], Kevlar[9], H_2O, hexane[10], and DCM[11] were
440 described by the all-atom optimized potential for liquid simulations (OPLS-AA)
441 force field[12, 13], which has been used successfully to get the structures and
442 properties of mixed systems of organic solvents and H_2O[14-17]. The parameters in
443 the OPLS-AA and electric state were determined using the PolyParGen
444 software[18, 19]. The nonbonding interactions between different atoms in the system
445 include both electrostatic and van der Waals terms. The former one was
446 calculated *via* the particle-particle-particle-mesh (PPPM) algorithm with an
447 accuracy of 0.0001. The latter one was computed by the 12-6 Lennard-Jones (LJ)
448 potential, which was truncated at 1.2 nm. The SHAKE algorithm[20] was applied
449 to O-H bonds to reduce high-frequency vibrations. The Lorentz-Berthelot mixing
450 rules were used to model the parameters between different atomic species. The
451 atomic structures of H_2O, DCM, PIP, hexane, and Kevlar are shown in Fig. S27.
452 All the MD simulations in this work were carried out with the large-scale
453 atomic/molecular massively parallel simulator (LAMMPS)[21]. The integration of the
454 Newtonian equations of motion uses a timestep of 1.0 fs, which has been
455 demonstrated to ensure energy conservation. In the MD simulations, all the
456 components were relaxed in the isothermal-isobaric (NPT) ensemble for 10 ns

with the temperature (T) of 298.15 K and the pressure (P) of 1.0 atm along all directions. The T and P are kept *via* the Nose-Hoover thermostat and Parrinello-Rahman barostat, respectively. Following the completion of the equilibration process for systems, we merged system ANF hydrogel and hexane to create the integrated system I (Fig. S29), and then we combined system ANF hydrogel and DCM to create the integrated system II (Fig. S29). The integrated system I and II exhibit an absence of periodicity in the *z*-direction. Then, all the components were relaxed in the microcanonical (NVE) thermodynamic ensemble with T of 298.15 K. After 30 ns, the MD simulation was in equilibrium, then run for a further 10 ns to collect data for the purpose of analyzing properties and structures.

To get the insight into trans-interface resistance of PIP from H_2O and Kevlar to hexane or DCM, we used umbrella sampling to calculate the PMF along the *z*-direction (-16.0 Å < Z < 16.0 Å), and further got the potential barrier for PIP crossing the interface. Simulated system III and IV were constructed for calculating PMF, which construction steps are like system I and II. The difference is the number of components (Table S7). The system III and IV were simulated with NVT thermodynamic ensemble at T = 298.15 K. Different sizes of sampling windows were used to ensure sufficient sampling, with a 0.5 Å interval window in the interface region (-4.0 Å < Z < 4.0 Å) and a 1.0 Å sampling window in other regions. A spring potential with the spring constant of 10 kcal mol^{-1} $Å^{-2}$ was applied to the PIP in each sampling window. Each sampling was carried out for up to 1,000,000 steps after each window was fully equilibrated, and each

step lasts 1.0 fs with a sampling interval of 0.1 ps. During the MD process, the PIP was initially fixed at the center of each sampling segment with a spring potential and then the simulations were operated to obtain the final equilibrium state for umbrella sampling. The weighted histogram analysis method (WHAM)[22] was then used to obtain the PMF curve.

The parameters of the bond, angle, dihedral, van der Waals interactions, and electrostatic interactions of PIP[8], Kevlar[9], H_2O, hexane[10], and DCM[11] were described by the all-atom optimized potential for liquid simulations force field[12, 13]. The molecular dynamics (MD) simulation process of system I and system II were carried out with the large-scale atomic/molecular massively parallel simulator (LAMMPS)[21], and the integration of the Newtonian equations of motion uses a timestep of 1.0 fs. In the process of MD simulations, all the components were relaxed in the isothermal-isobaric (NPT) ensemble for 10 ns with the temperature (T) of 298.15 K and the pressure (P) of 1.0 atm along all directions. The T and P are kept *via* the Nose-Hoover thermostat and Parrinello-Rahman barostat, respectively. Following the completion of the equilibration process for system ANF hydrogel, hexane and DCM, we merged system ANF hydrogel and hexane to create the integrated system I, and then combined system ANF hydrogel and DCM to create the integrated system II (Fig. S30). The integrated system I and II exhibit an absence of periodicity in the z-direction. Then, all the components were relaxed in the microcanonical (NVE) thermodynamic ensemble with T of

298.15 K. After 30 ns, the MD simulation was in equilibrium, then run for a further 10 ns to collect data for the purpose of analyzing properties and structures.

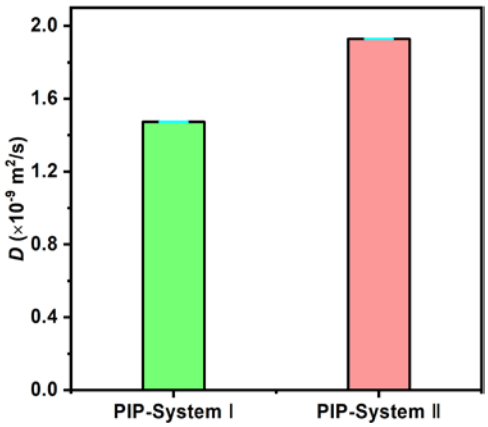

Fig. S32 Self-diffusion coefficient of PIP in two systems. Self-diffusion coefficient of PIP in system I (hexane as organic phase) and system II (DCM as organic phase)

5.3. Simulation details of potential of mean force (PMF)

Integrated systems III and IV were constructed for calculating PMF, which denotes a trans-interface resistance of PIP from H_2O and Kevlar to hexane or DCM. The construction steps are like system I and II, and the difference is the number of components (Table S7).

Specifically, individual systems including system ANF hydrogel, system hexane, and system DCM were constructed as the initial configurations with various numbers of components (Table S7). System III was consisted of system hexane (upper) and system ANF hydrogel (lower), and system IV was consisted of system DCM (upper) and system ANF hydrogel (lower).

Table S7 The number of H_2O, DCM, PIP, hexane, and Kevlar in composite systems.

Type	**H_2O**	**Kevlar**	**PIP**	**hexane**	**DCM**
System III	1330	5	1	185	/
System IV	1330	5	1	/	375

6. Other supplementary experiments

6.1. SEM images under various accelerating voltages

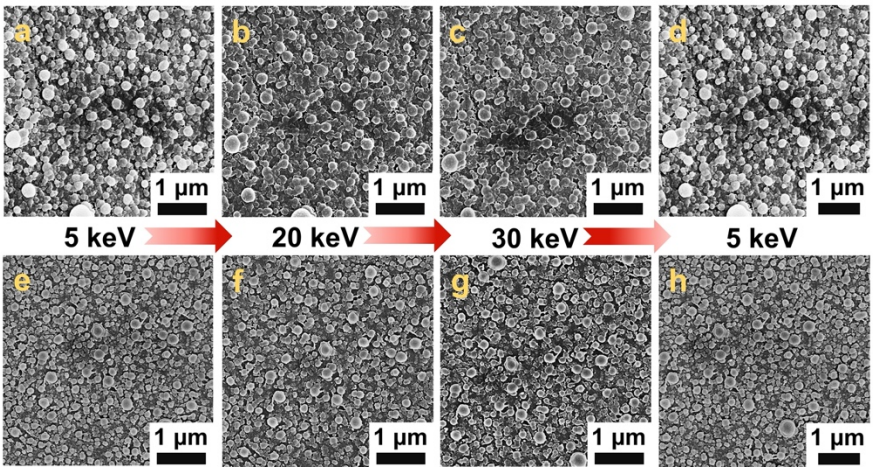

Fig. S33 SEM images of T5P4 and AcT5P4 membranes under various accelerating voltages. (a to d) T5P4 membranes. (e to h) AcT5P4 membranes.

6.2. IR tests and gas released experiments

6.2.1. In-situ temperature monitoring of IP

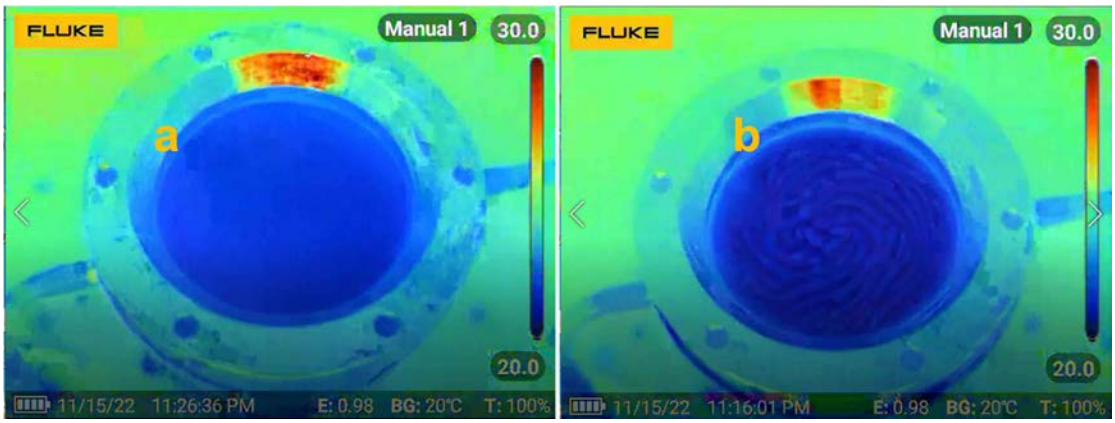

Fig. S34 In-situ captured changes in temperature during interfacial polymerization using IR camera. (**a**) hexane as organic solvent, (**b**) DCM as organic solvent. TMC: 0.5% w/v, PIP: 0.04% w/v.

529 **6.2.2. Gas releasing during IP process**

530 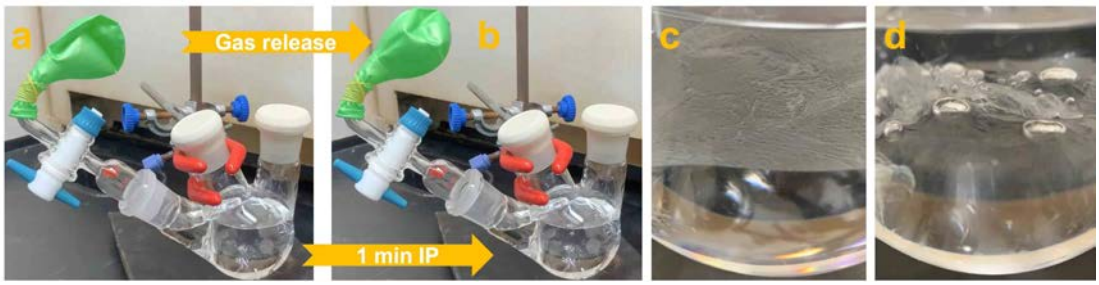

531 **Fig. S35 Gas released experiments.** (a, b) Inflation of a balloon by the released gas
532 during IP process. (c) PA film fabricated with hexane. (d) PA film fabricated with DCM.

533 Compared with the hexane system (Fig. S32c), a large amount of released gas was
534 trapped in the DCM system, leading to an obvious gas vapor deformed membrane.
535 Specifically, due to its higher density, layering DCM phase atop the water phase result
536 in a phase-inverted IP process compared to the conventional hexane system. This led to
537 the sinking of the DCM phase to the bottom, and the evaporation of DCM was hindered
538 by the aqueous phase. Meanwhile, the water phase evaporation war marginal, as the
539 temperature change (Fig. S31) caused by the released heat during IP was insufficient.
540 These findings firmly demonstrate the gas release process associated with the use of
541 DCM.

542 **6.3. Monomer diffusion process**

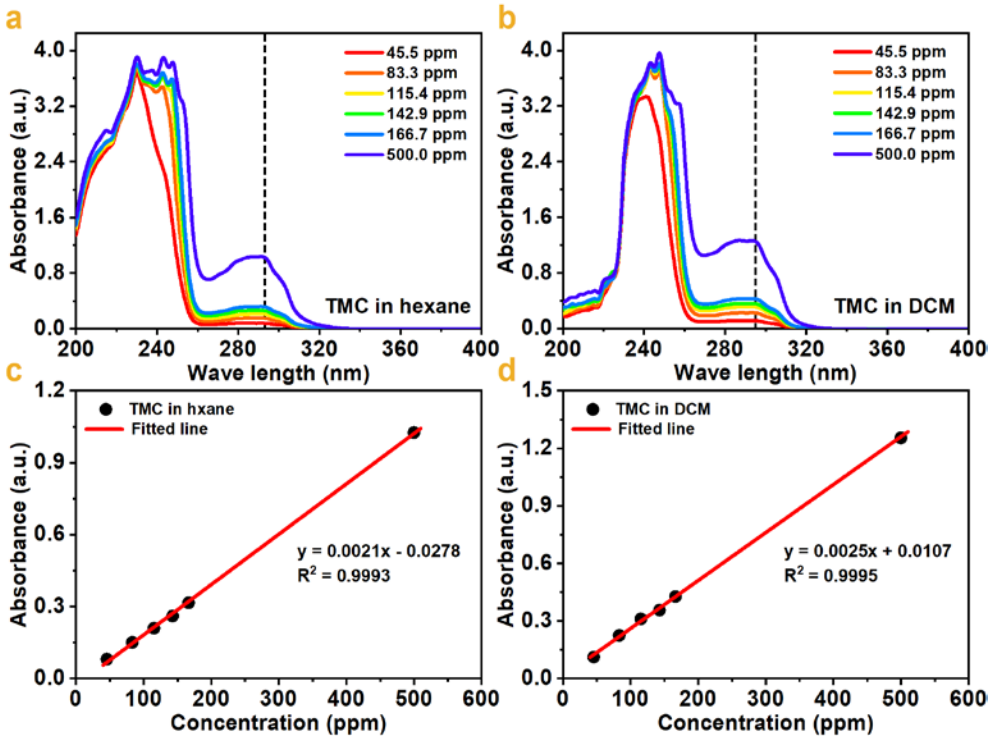

Fig. S36 UV-Vis spectra of TMC in hexane and DCM. UV-Vis absorbance of TMC in hexane (**a**) and DCM (**b**). Calibration curves of absorbance as a function of concentration of TMC in hexane (**c**) and DCM (**d**).

Table S8 UV-vis absorption peak of monomers in various solvents.

Monomer	**Solvent**	**UV absorption peak (nm)**
TMC	hexane	293
TMC	DCM	295
PIP	DI	217
PIP	hexane	273
PIP	DCM	231

Table S9 Detected TMC concentration in organic phase during 1 min diffusion.

	0 min	1 min	
Top TMC/hexane (0.5% w/v) Bottom DI	5000	4988 ± 10	TMC in hexane (ppm)
Top TMC/DCM (0.5% w/v) Bottom DI	5000	4921 ± 32	TMC in DCM (ppm)

The amount of TMC in DCM after 1 min diffusion experiment is comparable to that in hexane, which might denote a minor effect of the transport of TMC in IP process.

6.4. The effective pore size, pore size distribution and MWCO of TFC PA membranes based on ANF hydrogel

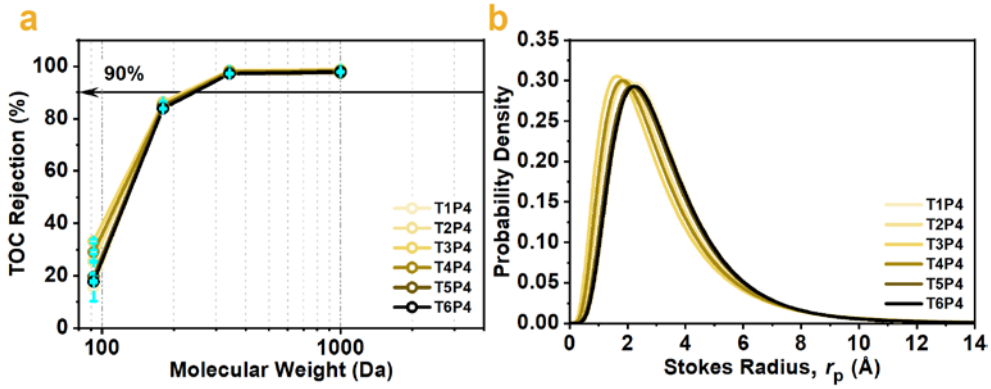

Fig. S37 MWCO and PDF of PA membranes prepared with DCM. (**a**) TOC rejection of neutral solutes. (**b**) Pore size distribution of the membranes estimated with data presented in (**a**) based on Supplementary Equation 1. The PA active layer was prepared with a constant PIP concentration (0.04% w v^{-1}) and the concentrations of TMC were varied at 0.1, 0.2, 0.3, 0.4, 0.5 and 0.6% w v^{-1}.

Table S10 The effective mean pore radius μ_p, geometric standard deviation σ_p and molecular weight cut-off (MWCO) of ANF-supported TFC membranes.

PA membranes						
Organic solvent for IP	**TMC Content (% w v^{-1})**	**PIP Content (% w v^{-1})**	**Solvent activation**	**μ_p (Å)**	**σ_p**	**MWCO (Da)**
DCM	0.1	0.04	/	2.982	1.673	229
DCM	0.2	0.04	/	2.711	1.782	222
DCM	0.3	0.04	/	2.483	1.913	225
DCM	0.4	0.04	/	2.633	1.834	232
DCM	0.6	0.04	/	2.960	1.696	242

563

564

565 **6.5. Zeta potential**

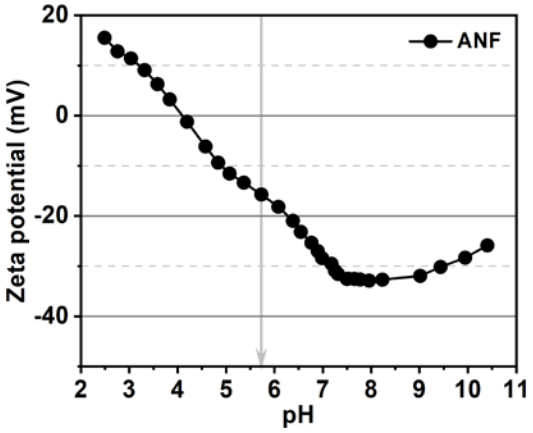

566

567 **Fig. S38 Surface zeta potential of ANF substrate**.

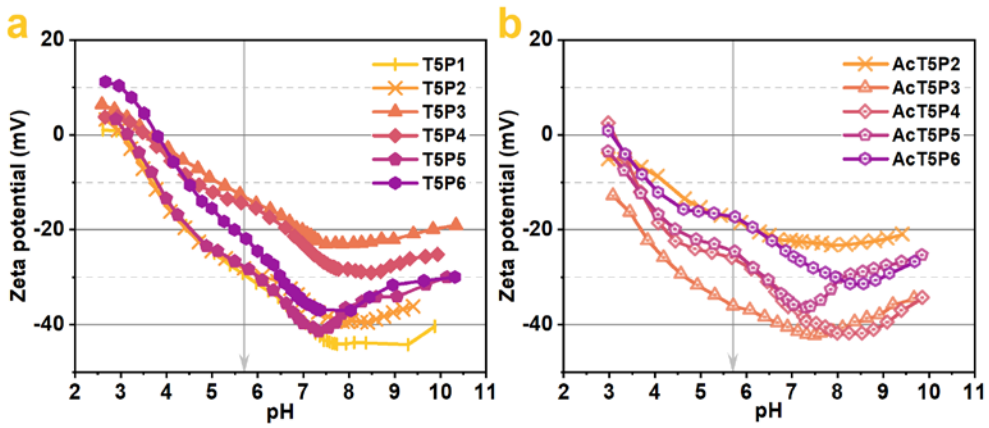

Fig. S39 Surface zeta potential of PA membranes prepared with DCM and subsequent solvent activation. (**a**) The PA active layer was prepared with a constant TMC concentration (0.5% w v^{-1}) and the concentrations of PIP were varied at 0.01, 0.02, 0.03, 0.04, 0.05, and 0.06% w v^{-1}. (**b**) The activated PA membranes was prepared with a constant TMC concentration (0.5% w v^{-1}) and the concentrations of PIP were varied at 0.02, 0.03, 0.04, 0.05, and 0.06% w v^{-1}.

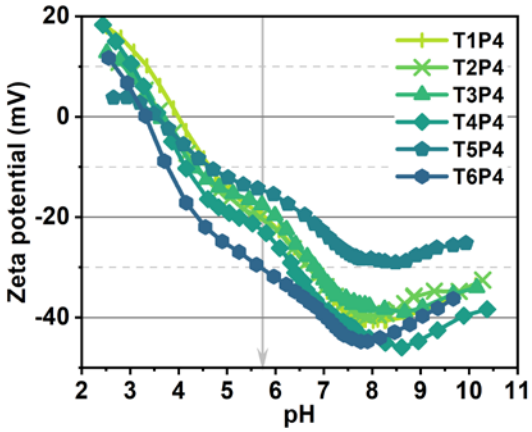

Fig. S40 Surface zeta potential of PA membranes prepared with DCM and subsequent solvent activation. The PA active layer was prepared with a constant PIP concentration (0.04% w v^{-1}) and the concentrations of TMC were varied at 0.1, 0.2, 0.3, 0.4, 0.5 and 0.6% w v^{-1}.

6.6. Positron annihilation Doppler broadening energy spectroscopy results

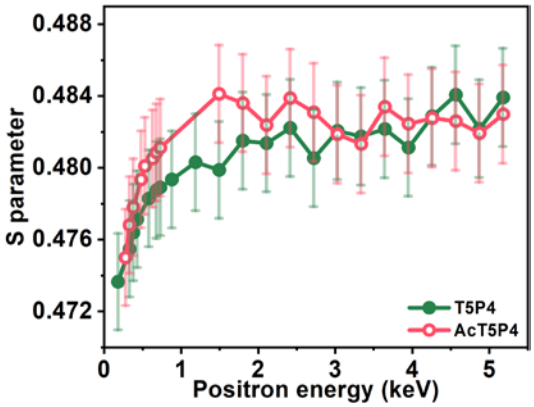

Fig. S41 S parameter of the selected TFC-PA membranes as a function of the positron energy. The curve with solid dot represents PA prepared with DCM and that with hollow dot represents PA prepared with DCM and subsequent activation. The corresponding TMC and PIP concentrations used for the IP reaction are 0.5% w v^{-1} and 0.04% w v^{-1}, respectively.

6.7. Pure water permeance of different substrates

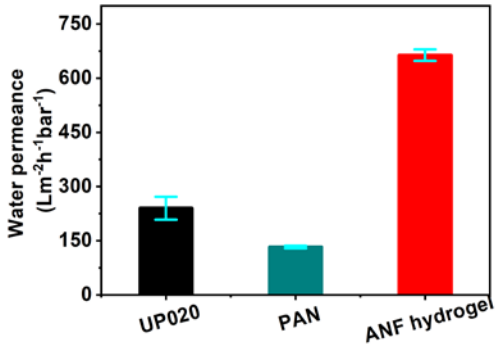

Fig. S42 Pure water permeance of substrates. UP020, PAN are two types of commercial substrates and ANF hydrogel substrate was prepared using a casting machine.

6.8. MWCO and pore size distribution of NF90 and NF270

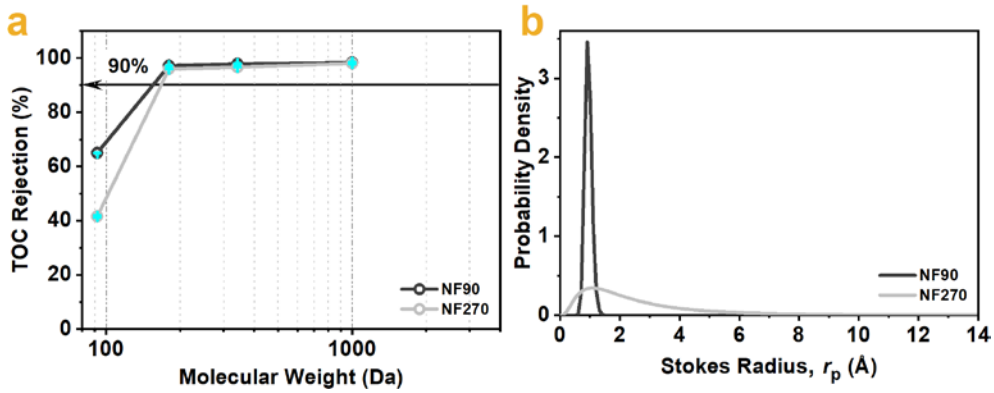

Fig. S43 MWCO and PDF of commercial TFC PA membranes. (**a)** Rejection of neutral solutes. (**b)** Pore size distribution of the TFC-PA membranes estimated with data presented in (**a**) based on Supplementary Equation 1.

598 **Table S11** The mean pore radius μ_p, geometric standard deviation σ_p and MWCO of

599 commercial TFC PA membranes.

Commercial Membranes	μ_p (Å)	σ_p	MWCO (Da)
NF90	0.912	3.808	155
NF270	2.002	2.203	167

600 **6.9. Ionized carboxyl group density of NF90 and NF270**

601 **Table S12** Ionized carboxyl density under various solution pH with a unit of sites nm^{-2}.

	NF90	NF270
pH 3.5	0.4 ± 0.0	0.6 ± 0.1
pH 7	0.9 ± 0.0	3.3 ± 0.1
pH 10.5	24.0 ± 0.7	39.0 ± 3.7

603 **6.10. Zeta potential**

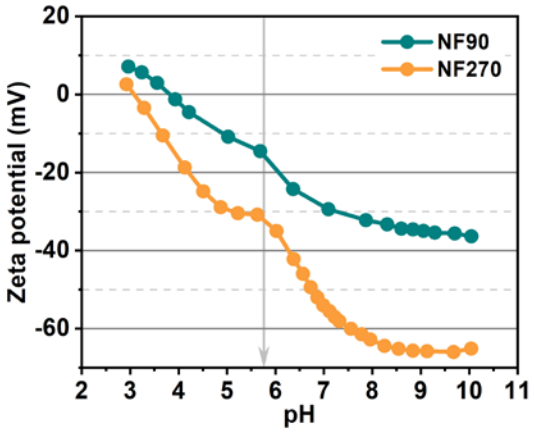

604

605 **Fig. S44 Surface zeta potential of commercial TFC PA membranes.**

606 **6.11. Solubility test**

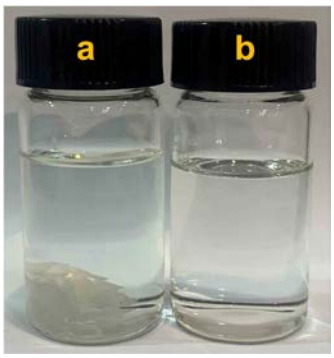

Fig. S45 (**a**) PIP was barely dissolved in hexane and (**b**) PIP was completely dissolved in DCM.

Table S13 Physical properties of the solvents.

		hexane	DCM	Water
Hildebrant solubility parameter	$(cal/mL)^{0.5}$	6.9	9.7	23.5
Dipole	D	0	1.14	1.87
Relative permittivity at 20°C		1.9	8.93	78
Absolute viscosity at 25°C	cP	0.31	0.44	1
Boiling point	°C	69	39	100
Vapor pressure	Torr	124	350	18
Specific heat capacity	$cal\ mol^{-1}\ K^{-1}$	42	24	18

7. Movie captions

Movie S1. PIP transportation at hexane/hydrogel interface.

Movie S2. PIP transportation at DCM/hydrogel interface.

Movie S3. In-situ temperature monitoring of IP.

8. References

(1) Xu L; Zhao X; Xu C, Kotov NA. Water-Rich Biomimetic Composites with Abiotic Self-Organizing Nanofiber Network. *Adv. Mater.* **2018**, *30* (1), 1703343.

(2) Sauerbrey G. Verwendung von Schwingquarzen zur Wägung dünner Schichten und zur Mikrowägung. *Z. Phys.* **1959**, *155* (2), 206-222.

(3) Chen G-E; Liu Y-J; Xu Z-L; Tang Y-J; Huang H-H, Sun L. Fabrication and characterization of a novel nanofiltration membrane by the interfacial polymerization of 1, 4-diaminocyclohexane (DCH) and trimesoyl chloride (TMC). *RSC Adv.* **2015**, *5* (51), 40742-40752.

(4) Aimar P; Meireles M, Sanchez V. A contribution to the translation of retention curves into pore size distributions for sieving membranes. *J. Membr. Sci.* **1990**, *54* (3), 321-338.

(5) Chen D; Werber JR; Zhao X, Elimelech M. A facile method to quantify the carboxyl group areal density in the active layer of polyamide thin-film composite membranes. *J. Membr. Sci.* **2017**, *534*, 100-108.

(6) Martínez L; Andrade R; Birgin EG, Martínez JM. PACKMOL: A package for building initial configurations for molecular dynamics simulations. *J. Comput. Chem.* **2009**, *30* (13), 2157-2164.

(7) Berendsen H; Grigera J, Straatsma T. The missing term in effective pair potentials. *J. Phys. Chem.* **1987**, *91* (24), 6269-6271.

(8) Farmahini AH; Kvamme B, Kuznetsova T. Molecular dynamics simulation studies of absorption in piperazine activated MDEA solution. *Phys. Chem. Chem. Phys.* **2011**, *13* (28), 13070-13081.

(9) Yuan S; Zhang G; Zhu J; Mamrol N; Liu S; Mai Z; Van Puyvelde P, Van der

Bruggen B. Hydrogel assisted interfacial polymerization for advanced nanofiltration membranes. *J. Mater. Chem. A* **2020**, *8* (6), 3238-3245.

(10) Wen Y; Dai R; Li X; Zhang X; Cao X; Wu Z; Lin S; Tang CY, Wang Z. Metal-organic framework enables ultraselective polyamide membrane for desalination and water reuse. *Sci. Adv.* **2022**, *8* (10), eabm4149.

(11) Liu Z; Timmermann J; Reuter K, Scheurer C. Benchmarks and dielectric constants for reparametrized OPLS and polarizable force field models of chlorinated hydrocarbons. *J. Phys. Chem. B* **2018**, *122* (2), 770-779.

(12) Canongia Lopes JN, Pádua AA. Molecular force field for ionic liquids composed of triflate or bistriflylimide anions. *J. Phys. Chem. B* **2004**, *108* (43), 16893-16898.

(13) Wang X; Chen F; Girard GM; Zhu H; MacFarlane DR; Mecerreyes D; Armand M; Howlett PC, Forsyth M. Poly (ionic liquid) s-in-salt electrolytes with co-coordination-assisted lithium-ion transport for safe batteries. *Joule* **2019**, *3* (11), 2687-2702.

(14) Vishnyakov A; Lyubartsev AP, Laaksonen A. Molecular dynamics simulations of dimethyl sulfoxide and dimethyl sulfoxide− water mixture. *J. Phys. Chem. A* **2001**, *105* (10), 1702-1710.

(15) Plazzer MB; Henry DJ; Yiapanis G, Yarovsky I. Comparative study of commonly used molecular dynamics force fields for modeling organic monolayers on water. *J. Phys. Chem. B* **2011**, *115* (14), 3964-3971.

(16) Mushrif SH; Caratzoulas S, Vlachos DG. Understanding solvent effects in the selective conversion of fructose to 5-hydroxymethyl-furfural: a molecular dynamics investigation. *Phys. Chem. Chem. Phys.* **2012**, *14* (8), 2637-2644.

(17) Zubillaga RA; Labastida A; Cruz B; Martínez JC; Sanchez E, Alejandre J. Surface tension of organic liquids using the OPLS/AA force field. *J. Chem. Theory Comput.* **2013**, *9* (3), 1611-1615.

(18) Grünewald F; Alessandri R; Kroon PC; Monticelli L; Souza PC, Marrink SJ. Polyply; a python suite for facilitating simulations of macromolecules and nanomaterials. *Nat. Commun.* **2022**, *13* (1), 68.

(19) YABE M; MORI K; UEDA K, TAKEDA M. Development of PolyParGen software to facilitate the determination of molecular dynamics simulation parameters for polymers. *J. Comput. Chem., Jpn.* **2019**, *5*, 2018-0034.

(20) Ryckaert J-P; Ciccotti G, Berendsen HJ. Numerical integration of the cartesian equations of motion of a system with constraints: molecular dynamics of n-alkanes. *J. Comput. Phys.* **1977**, *23* (3), 327-341.

(21) Plimpton S. Fast parallel algorithms for short-range molecular dynamics. *J. Comput. Phys.* **1995**, *117* (1), 1-19.

(22) Kumar S; Rosenberg JM; Bouzida D; Swendsen RH, Kollman PA. The weighted histogram analysis method for free-energy calculations on biomolecules. I. The method. *J. Comput. Chem.* **1992**, *13* (8), 1011-1021.